Current Biology 20, 1499–1510, September 14, 2010 ©2010 Elsevier Ltd All rights reserved DOI 10.1016/j.cub.2010.06.075

Article

Sequential Activation of Apical and Basolateral Contractility Drives Ascidian Endoderm Invagination

Kristin Sherrard,[1,3,5] François Robin,[2,3,5] Patrick Lemaire,[2,4,*] and Edwin Munro[1,4,5,*]

[1]Center for Cell Dynamics, Friday Harbor Laboratories, 620 University Road, Friday Harbor, WA 98250, USA

[2]IBDML, UMR6216 CNRS/Université de la Méditerrannée, Case 907, Campus de Luminy, F-13288 Marseille cedex 9, France

Summary

Background: Epithelial invagination is a fundamental morphogenetic behavior that transforms a flat cell sheet into a pit or groove. Previous studies of invagination have focused on the role of actomyosin-dependent apical contraction; other mechanisms remain largely unexplored.

Results: We combined experimental and computational approaches to identify a two-step mechanism for endoderm invagination during ascidian gastrulation. During Step 1, which immediately precedes invagination, endoderm cells constrict their apices because of Rho/Rho-kinase-dependent apical enrichment of 1P-myosin. Our data suggest that endoderm invagination itself occurs during Step 2, without further apical shrinkage, via a novel mechanism we call collared rounding: Rho/Rho-kinase-independent basolateral enrichment of 1P-myosin drives apico-basal shortening, whereas Rho/Rho-kinase-dependent enrichment of 1P and 2P myosin in circumapical collars is required to prevent apical expansion and for deep invagination. Simulations show that boundary-specific tension values consistent with these distributions of active myosin can explain the cell shape changes observed during invagination both in normal embryos and in embryos treated with pharmacological inhibitors of either Rho-kinase or Myosin II ATPase. Indeed, we find that the balance of strong circumapical and basolateral tension is the only mechanism based on differential cortical tension that can explain ascidian endoderm invagination. Finally, simulations suggest that mesectoderm cells resist endoderm shape changes during both steps, and we confirm this prediction experimentally.

Conclusions: Our findings suggest that early ascidian gastrulation is driven by the coordinated apposition of circumapical and lateral endoderm contraction, working against a resisting mesectoderm. We propose that similar mechanisms may operate during other invaginations.

Introduction

Invagination, in which a sheet of epithelial cells bends inwards to form a pit or groove, is a fundamental building block of morphogenesis used throughout animal development. Although it is one of the simplest deformations that a sheet of cells can perform, the cellular and mechanical bases for invagination remain poorly understood. Invagination necessarily involves a change in the shape of participating cells from columnar to wedge-shaped, with a reduced apex and an expanded base. The challenge has been to determine the molecular origins and distributions of forces that cause these cell shape changes and to understand how these forces are integrated to produce global changes in tissue geometry.

Many potential force-generating mechanisms for invagination have been proposed (reviewed in [1, 2]). These include localized differences in adhesivity or in local cortical actomyosin contractility, or cell shape changes driven by internal cytoplasmic microtubules. In addition, tissue-extrinsic forces—e.g., swelling of an extracellular gel or active spreading (epiboly) of neighboring tissues—could cause a tissue to buckle inward. Computer simulations have shown that under suitable conditions each of these modes of force generation could drive invagination [1–6]. However, direct experimental support for most of these hypothesized mechanisms remains weak.

The best-studied cellular behavior associated with invagination is apical constriction, in which cells actively shrink their apical surfaces. Studies in *Drosophila*, sea urchins, *Xenopus*, and mice support an active role for actomyosin contractility in driving apical constriction [7–11]. Apical enrichment of myosin that has been activated by phosphorylation of the regulatory light chain on serine 19 accompanies apical constriction in all of these cases. Upstream regulators of this enrichment include, but are not limited to, Rho GTPases, and pharmacological or genetic inhibition of apical myosin phosphorylation prevents most invaginations [8, 9, 12–14]. The success in documenting the occurrence, necessity, and control of apical constriction in many systems has led to its widespread acceptance as the major cause of invagination.

Although apical constriction clearly contributes to many invaginations, it cannot provide a complete explanation of the phenomenon (reviewed in [15, 16]). The main phase of apical constriction usually precedes invagination. Invagination itself is often accompanied by a marked apico-basal *shortening* and it has been suggested that active apico-basal shortening could be an important driving force for invagination, but this hypothesis has not been explored experimentally, nor has a molecular or genetic basis for apico-basal shortening been identified [15, 17]. More generally, the extent to which apical constriction causes a tissue to invaginate will depend on the distributions of other tissue-intrinsic forces and on the extent to which surrounding tissues either help or resist deformation.

Here, we focus on the very simple case of endoderm invagination in ascidians (Urochordata), in which a monolayer plate of just 10 cells invaginates to internalize a primitive gut rudiment in an embryo of ~100 cells. This process is ideally suited for exploring the cytomechanical basis for invagination [18]. Ascidians have small optically clear embryos, making it possible to do comprehensive three-dimensional analysis of cellular shape change from live and fixed embryos [19]. Their stereotyped early development, based on an invariant lineage [20], provides a high-resolution timeline to the ~45 min

*Correspondence: lemaire@ibdml.univ-mrs.fr (P.L.), emunro@uchicago.edu (E.M.)

[3]These authors contributed equally to this work

[4]These authors contributed equally to this work

[5]Present address: Department of Molecular Genetics and Cell Biology, 920 E 58th St, Chicago, Il 60637, USA

process. Finally, the small cell numbers mean that computer simulations can relate force-generating mechanisms within individual cells to the tissue- and embryo-level deformations that they cause.

Combining 4D microscopy, experimental manipulation of actomyosin contractility, and computer simulation, we show that sequential deployment of active myosin to different endoderm cell surfaces is tightly phased with, and could drive, a 2-step sequence of endoderm cell shape changes during invagination. Our results suggest that apical constriction alone cannot explain either step: during Step 1, both apical endoderm constriction and ectoderm epiboly contribute to shaping a tall apically narrow endoderm plate. During Step 2, it is the interplay between circumapical and basolateral endoderm tensions, driving apico-basal shortening around tightly maintained, preshrunk apices, that causes invagination itself.

Results

4D Morphometric Analysis Shows that Endoderm Invagination Occurs in Two Distinct Steps

We began by analyzing 3D reconstructions made from serial confocal micrographs of fixed embryos during early gastrulation (between the 64- and 112-cell stages; Figure 1A, Figure S1 available online). A comparative analysis of four different species (*Ciona intestinalis, C. savignyi, Phallusia mammillata*, and *Boltenia villosa*; Figures 1B–1D) reveals a core sequence of cell shape changes that are tightly phased with the conserved pattern of cell divisions.

At the 64-cell stage, embryos are approximately spherical; animal and vegetal cells are equal in height and there is a very small blastocoel. Between the 64- and early 112-cell stages (lasting ~30 min; left three columns in Figures 1B–1D), the vegetal endoderm plate flattens and shrinks its apical surface. The animal hemisphere spreads as cells shorten apico-basally (64- to 76-cell stages), then divide (76- to early 112-cell stage). From early to late 112-cell stage (lasting ~15 min; rightmost two columns in Figures 1B–1D), the presumptive endoderm cells invaginate, as the whole embryo bends inward on the vegetal side to form a pit centered on the vegetal pole. Invagination is followed immediately by endoderm cell cleavage, and then involution of the anterior notochord and lateral muscle primordia ([21] and not shown). We observed the same sequence of events in all four species with only minor variations (Figures 1B–1D and data not shown; see legend for details). The entire sequence occurs without disruption of the epithelial nature of the endodermal plate, as shown by the constant presence of ZO-1-positive tight junctions (Figures S2A–S2D), and without cell rearrangements. Thus invagination is driven solely by the cumulative effect of individual cell shape changes.

To more precisely characterize the cell shape changes that accompany invagination, we used 3D Virtual Embryo software [19] to reconstruct and quantify the shapes of all cells in fixed *Ciona intestinalis* embryos (Figures 2A–2I). Between the 64- and early 112-cell stages, most blastomeres underwent significant shape changes (Figures 2A and 2B) that were different for each hemisphere, but common to cells within a hemisphere. The apico-basal heights of vegetal cells first increased up to the 76-cell stage and then shortened slightly (Figures 2D and 2E). In parallel, the apices of vegetal cells shrunk, whereas those of animal cells remained stable or slightly increased (Figures 2G and 2H). There was also a slight but significant decrease in endoderm cell volume during

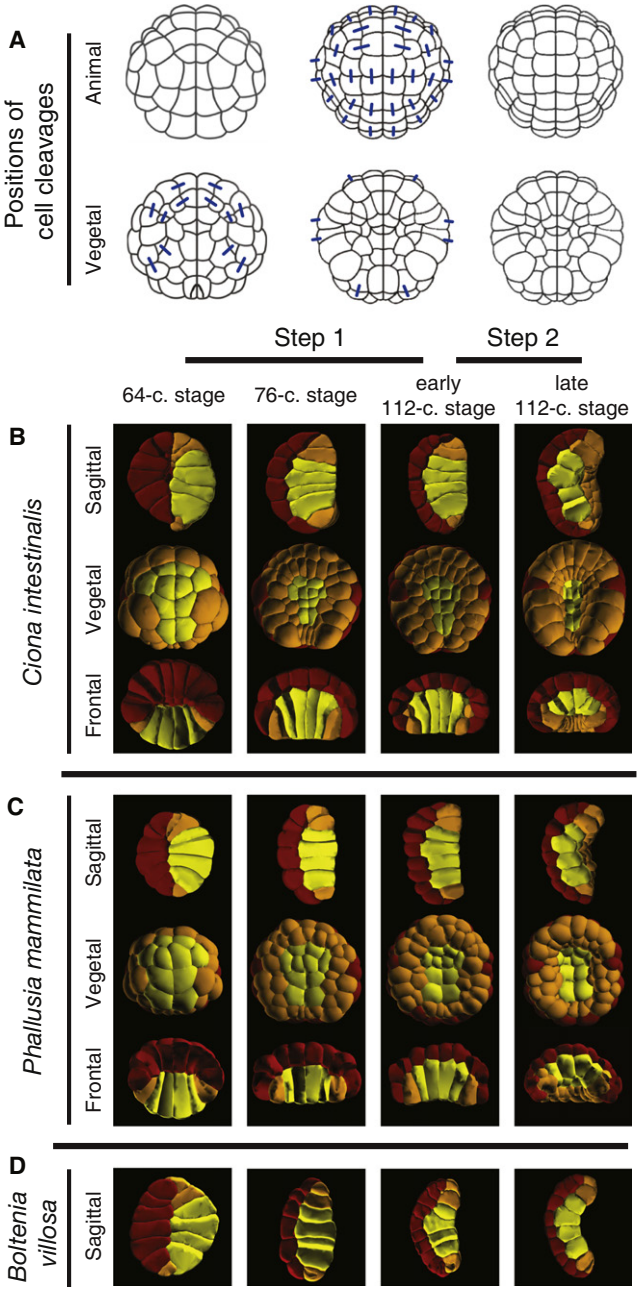

Figure 1. Ascidian Invagination Occurs in Two Highly Conserved Steps

(A) Animal (top) and vegetal (bottom) views of *Ciona* embryos showing the positions of cell cleavages between the 64- and 76-cell (early Step 1, left), 76- and early 112-cell (late Step 1, center), and early/late 112-cell (Step 2, right) stages. Blue bars link newly formed sister cell pairs.

(B–D) Sagittal, vegetal, and frontal views of 3D-reconstructed *Ciona intestinalis* (B), *Phallusia mammillata* (C), and *Boltenia villosa* (D, sagittal only) embryos at the indicated stages. Yellow, endoderm; orange, mesoderm; red, ectoderm.

Figure S1 shows interactive 3D views of reconstructed embryos.

Step 1 (Figure S2E). The pattern of cell shape changes was dramatically different during the 112-cell stage. During this period, cell deformations were largely restricted to the central part of the vegetal plate (Figure 2C) and were most pronounced in the 10 endodermal precursors, which dramatically shortened apico-basally (Figure 2F), while slightly expanding

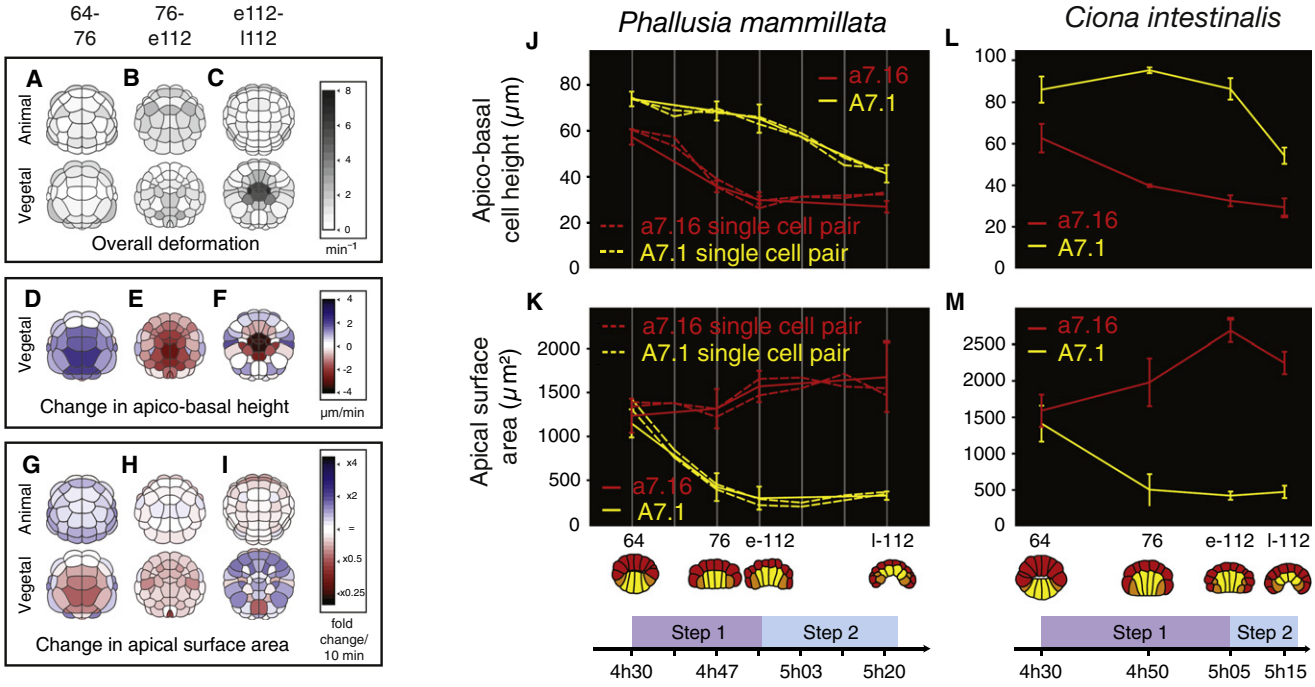

Figure 2. Morphometric Analysis of Cell Shape Changes during Invagination

(A–I) Changes in cell geometry across whole *Ciona intestinalis* embryos between the 64- and late 112-cell stages. Color scales indicate both magnitude and direction of changes (n = 3 embryos for 64-, 76-, and late 112-cell stages; n = 2 for early 112-cell stage).

(J and K) Measurements of apico-basal height (J) and apical surface area (K) for A7.1 (dashed yellow lines) and a7.16 (dashed red lines) cell pairs in reconstructed *Phallusia* embryos, imaged live every 5 min (each dashed line is an embryo), or fixed prior to imaging (solid lines, n = 7 embryos per data point; error bars are standard deviations).

(L and M) Measurements for the same cell pairs in fixed *Ciona intestinalis* embryos (n = 5 embryos per data point).

See Figure S2 for additional data on cell volume change and maintenance of epithelial architecture during invagination. Movie S1 and Movie S2 show time-lapse sequences of invagination.

their apices (Figure 2I) and maintaining constant volume (Figure S2E).

To characterize this further, we performed high-resolution 4D live microscopy on the transparent embryos of *Phallusia* focusing on representative vegetal (A7.1, endoderm precursor) and animal (a7.16, epidermis precursor) blastomeres. Significantly, we observed sharp transitions in the direction and/or magnitude of changes in apical surface area and apico-basal height for both animal and vegetal precursors that coincided with the onset of invagination (Figures 2J and 2K, dotted lines). Analogous trajectories for A7.1 and a7.16 were observed in *Boltenia* (Figure 1D; Movie S1) and *Ciona* (Figures 2L and 2M; Movie S2) embryos, although the lesser transparency of these embryos precluded a full characterization of cell shape changes in 3D.

We conclude that ascidian endoderm invagination occurs in two well-defined and evolutionary conserved steps, characterized by distinct patterns of underlying cell behavior. During Step 1, endoderm cells shrink their apical surface while the vegetal surface flattens, and the mesectoderm spreads and cleaves laterally. During Step 2, the endoderm cells shorten rapidly along their apico-basal axis with no further apical shrinkage while their basal ends expand and the vegetal plate invaginates.

Steps 1 and 2 Correlate with Distinct Patterns of Active Myosin Accumulation

To distinguish potential roles for microtubules and the actin cytoskeleton, we examined gastrulation in ascidian embryos treated with nocodazole or cytochalasin D to depolymerize microtubules and actin, respectively. Embryos treated with 1.3 µM nocodazole at the 64-cell stage stopped dividing, although cycles of nuclear division persisted (data not shown), but underwent a characteristic two-step invagination as deep as controls (Figure S3A and data not shown). Thus neither microtubules, nor cell shape changes associated with mesectoderm cell cleavages, are required for invagination. In contrast, embryos treated with 1 µM cytochalasin did not invaginate (data not shown), pointing to a role for the actin cytoskeleton.

A likely role for filamentous actin in invagination is to support actomyosin contractility. In nonmuscle cells, actomyosin contractility is activated by phosphorylation of the myosin II regulatory light chain at either the ser19 position (1P-myosin) or at the ser19 and thr18 positions (2P-myosin) [22]. 1P-myosin is primarily enriched within short-lived and rapidly changing structures such as cleavage furrows [23], whereas 2P-myosin is restricted to more persistent contractile structures such as stress fibers [24, 25].

Immunostaining embryos with 1P- and 2P-myosin antibodies revealed dynamic patterns of localization (Figures 3 and 4; Movie S3 and Movie S4). 1P-myosin was enriched circumapically in all cells during both steps and also on cleavage furrows (arrowheads in Figure 3). During Step 1, 1P-myosin was weakly detectable on the lateral surfaces of endoderm precursors and strongly enriched on their shrinking apical surfaces (Figures 3A, 3B, 3D, and 3E; Movie S3). Strikingly, in early Step 2, when endoderm cells transition from apical

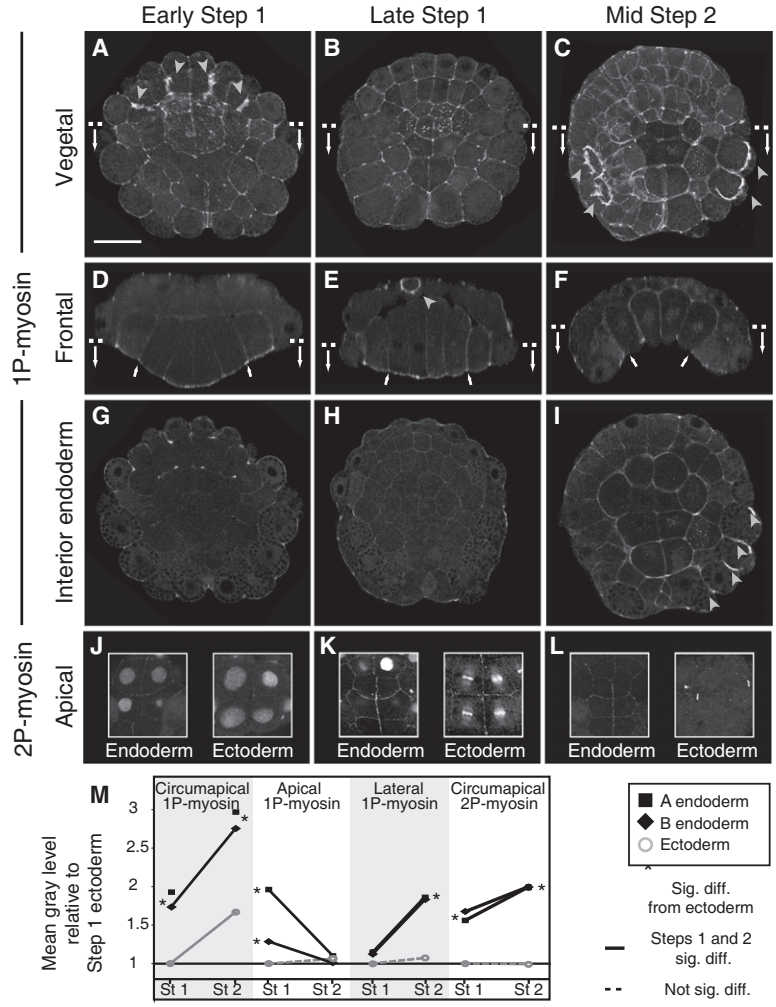

Figure 3. Patterns of Phosphomyosin Accumulation Correlate with Cell Shape Changes during Invagination

(A–I) Vegetal surface views (A–C), frontal sections (D–F), and horizontal sections (G–I) of *Boltenia* embryos showing 1P-myosin distribution at early and late Step 1 and mid Step 2. Dashed lines in (A)–(C) and (D)–(F) show positions of frontal and horizontal sections, respectively. Gray arrowheads in (A)–(C), (I): accumulation of 1P-myosin in cleavage furrows. White arrows in (D)–(F): lateral boundaries of endoderm plate.

(J–L) Circumapical 2P-myosin distributions on endoderm and ectoderm cells at early (J) and late (K) Step 1 and mid Step 2 (L). The cortical stain was confined to a narrow subapical region. Endoderm/ectoderm image pairs come from the same embryo. The antibody to 2P-myosin also labels nuclei and spindle midbodies as seen previously in other cell types [45]. See Movie S4 for 3D views of 2P-myosin.

(M) Quantification of relative pixel intensities (Step 1 versus Step 2; endoderm versus ectoderm) for different boundaries from fixed, immunostained *Boltenia* embryos. Asterisks indicate significant differences ($p < 0.05$ for 1-tailed Mann-Whitney U-tests; p was usually < 0.0001) between endoderm and ectoderm. Similar results for *Ciona* are presented in Figure 4. See Movie S3 and Movie S4 for 3D views of 1P-and 2P-myosin-stained embryos.

shrinkage to apico-basal shortening, 1P-myosin rapidly *disappeared* from the apical surfaces and accumulated strongly on the basal and lateral surfaces of all and only the endoderm cells (Figures 3C, 3F, and 3I). Meanwhile, 2P-myosin gradually accumulated circumapically on the endoderm precursors throughout Step 1 and persisted in Step 2 (Figures 3J–3M; Movie S4), whereas the ectoderm precursors weakly accumulated circumapical 2P-myosin only during late Step 1 (Figure 3K). Quantitative analysis of fluorescence intensities during Steps 1 and 2 supports these observations (Figure 3M). Thus 1P-myosin was always enriched on the endodermal cell surfaces undergoing shrinkage (apical in Step 1, basolateral during Step 2) whereas circumapical enrichment of 2P-myosin was associated with maintenance of small endoderm apices. These distributions are consistent with a direct role for myosin II in causing the forces that drive ascidian invagination.

RhoA-Dependent and -Independent Forms of Myosin II Activity Are Required for Cell Shape Changes during Both Steps of Invagination

To further assess the requirement for myosin II activity during invagination, we examined embryos treated at different time points during invagination with blebbistatin, a small molecule inhibitor of myosin II activity [26]. In embryos treated from the 64-cell stage (as in Figure 1B, left column) and fixed at late Step 1, we observed a significant reduction in apical endoderm shrinkage relative to paired controls (Figures 4A, 4B, and 4E), accompanied by a decrease in both endoderm and mesectoderm cell heights and an overall flattening of the embryo (Figures 4A, 4B, and 4F). By contrast, in embryos treated with blebbistatin from late Step 1 and fixed near the end of Step 2, we observed a significant reduction in apico-basal shortening and invagination of the endoderm, accompanied by a slight broadening of endoderm cell apices (Figures 4C–4F). Thus, myosin activity is required both for apical shrinkage during Step 1 and for apico-basal shortening and invagination during Step 2.

In other cases of apical constriction and invagination, myosin is activated by RhoA, in part through Rho-kinase, which phosphorylates the myosin regulatory light chain [12, 13]. To test a role for Rho GTPases in ascidian endoderm invagination, we microinjected embryos with point mutated, dominant-negative versions of RhoA, Cdc42, and Rac1. Dominant-negative RhoA-injected embryos failed to invaginate (Figure S3B). Surprisingly, in these embryos, apicobasal shortening of endoderm during Step 2 occurred with the same timing as in controls, suggesting that it is under the control of a distinct pathway (data not shown). In contrast, injecting dominant-negative forms of Cdc42 and Rac1 had no effect on invagination (not shown).

To test whether RhoA controls invagination via Rho kinase, we examined embryos treated with Y-27632, a specific pharmacological inhibitor of this kinase [27], at different times during invagination (Figures 4G–4R). Embryos treated with 100 μm Y-27632 from the early 64-cell stage on (Figure 1B, left column) and fixed at the end of Step 1 showed a reduction in endoderm apical shrinkage, a slight increase in endoderm cell heights, and incomplete flattening relative to paired controls (Figures 4G–4L). In embryos treated with 100 μm Y-27632 from the early 64-cell stage and fixed at the end of Step 2, apico-basal shortening occurred normally (Figure 4H), but the endoderm apices expanded during Step 2 (Figure 4G) and invagination was reduced (Figure 4N). To test a specific

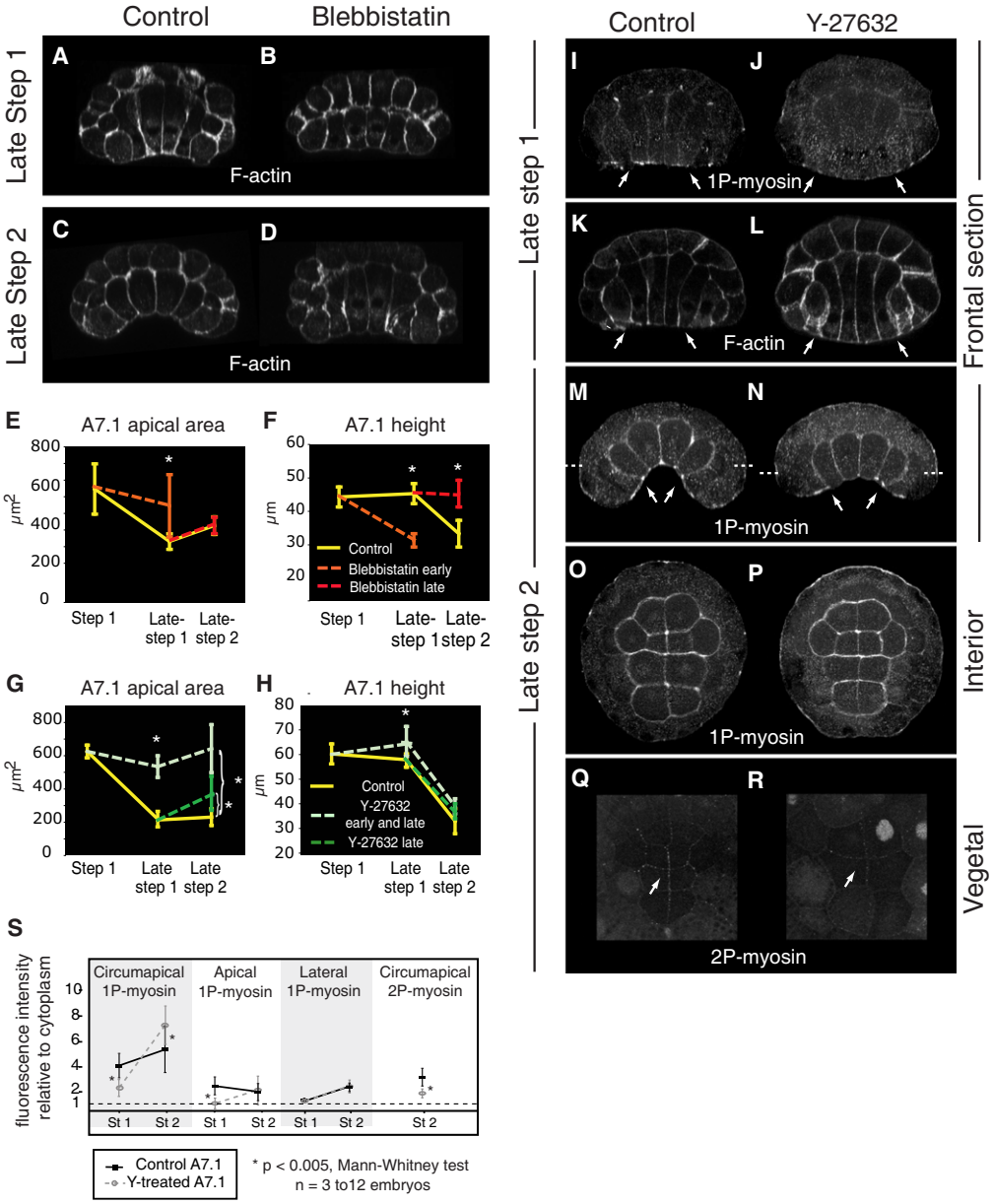

Figure 4. Different Zones of Localized Contractility Contribute to Invagination in *Ciona savignii*

(A–D) Cross-sectional views of embryos treated with 100 μM Blebbistatin during Step 1 (B) or Step 2 (D), fixed at the end of each step and phalloidin stained. (A and C) Controls for Step 1 and Step 2.

(E–H) Apical surface area (E, G) and apico-basal height (F, H) of A7.1 blastomere pairs at early Step 1, late Step 1, and late Step 2 in *Ciona savignii* embryos treated with 100 μM Blebbistatin (E, F) or 100 μM Y-27632 (G, H). Dashed lines link data points at the onset, intermediate time points, and end of each treatment. Measurements for paired WT controls shown in solid yellow lines. Asterisks in (E)–(H) indicate significant differences (asterisks indicate $p < 0.05$ for 2-tailed t test); error bars indicate standard deviations. Numbers of embryos measured were: Blebbistatin: $n \geq 7$ for all measurements; Y-27632: n = 4 and n = 5 for Step 2 control and Y-treated embryos, respectively, $n \geq 7$ for all other measurements. Embryos in (G), (H), (E), and (F) were fixed at a slightly different times during late Step 2.

(I–R) Phalloidin (K, L), 1P-myosin (I, J, M–P), and 2P-myosin (Q, R) staining in controls and in embryos treated with 100 μM Y-27632 for 30 min and fixed at the end of Step 1 (I–L) or Step 2 (M–R).

(I–N) Frontal sections.

(O and P) Horizontal sections along the lines indicated in (M) and (N).

(Q and R) Blow-up of subapical horizontal sections across the vegetal pole. Arrows indicate lateral cell-cell boundaries within the endoderm plate.

(S) Comparison of phosphomyosin levels on the indicated surfaces of A 7.1 cells in controls (solid black lines) and in embryos treated with 100 μM Y-27632 for 30 min prior to fixation at end of either Step 1 or Step 2 (light dashed lines). Figure S3 shows the effects on invagination of microtubule depolymerization and dominant-negative inhibition of RhoA. Movie S5 documents apical expansion during Step 2 in Y-treated embryos.

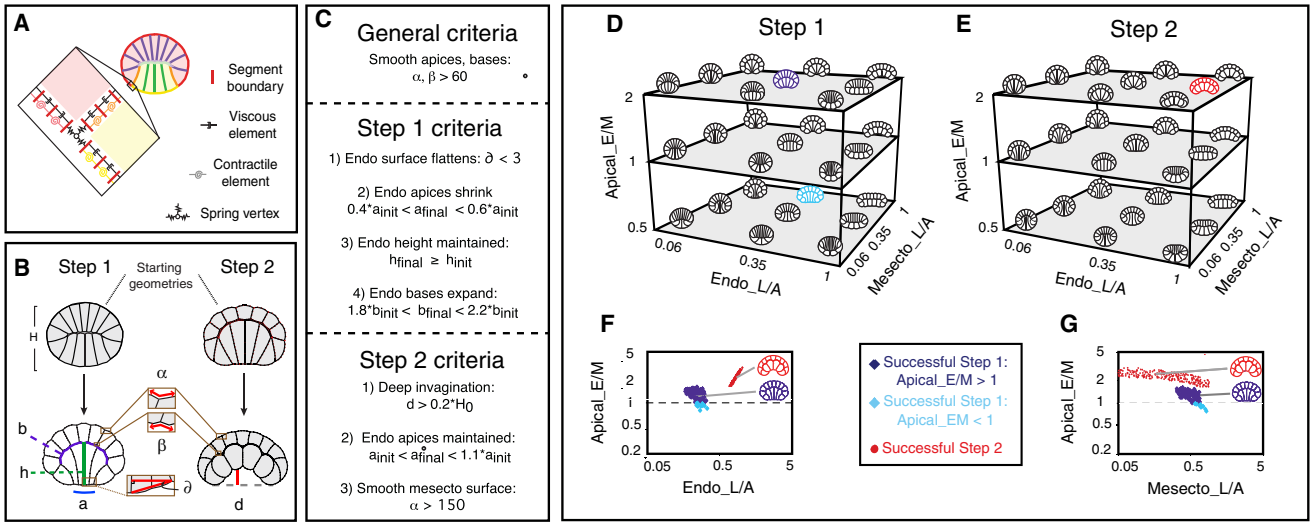

Figure 5. Simulations Based on Differential Cortical Tension Support a Two-Step Mechanism for Endoderm Invagination

(A) A model embryo constructed from contractile/viscoelastic elements. Different boundary colors indicate boundary-specific tension values.

(B) Starting and sample end geometries.

(C) Criteria used to specify passing geometries for Step 1 and Step 2 simulations of "wild-type" ascidian embryos. Symbols are represented in (B).

(D and E) Summary view of how final geometries attained by simulation from initial Step 1 (D) and Step 2 (E) geometries vary as a function of tension ratios. Colored embryos correspond to tension ratios lying nearest the clouds of passing parameter sets shown in (F) and (G).

(F and G) Position in tension ratio space of successful solutions shown as projections along the Mesecto_L/A (F) or Endo_L/A (G) axes. Values vary logarithmically along both axes and the central color legend applies to both panels.

See Supplementary Modeling Procedures for details. Movie S6 and Movie S7 show examples of successful Step 1 and 2 simulations. Figure S4 shows distributions of absolute tensions for Step 1 and 2 parameter space searches, and the results of parameter space searches with (a) boundary-specific internal viscosities and (b) unconstrained variation of basal tensions.

requirement for Rho-kinase during Step 2, we applied 100 μM Y-27632 from the end of Step 1 and examined embryos at the end of Step 2. Again, we observed apical expansion and reduced invagination with no effect on apico-basal shortening (Figures 4G and 4H, dark green; Figures 4M and 4N; Movie S5). Consistent with these phenotypes, 1P-myosin was lost on the endoderm apices of Y-treated embryos during Step 1 (compare Figures 4K, 4L, and 4S), as was circumapical 2P-myosin during Step 2 (Figures 4Q–4S). However, basolateral accumulation of 1P-myosin during Step 2 was unaffected in Y-treated embryos (Figures 4M–4P and 4S).

We conclude that at least two pathways differentially control myosin activation during ascidian gastrulation: A Rho-dependent pathway controls apical and circumapical accumulation of 1P- and 2P-myosin and is required for apical constriction and flattening during Step 1 and to prevent apical expansion during Step 2. A second pathway, which is Rho independent, or at least shows only weak dependence on Rho signaling, controls basolateral recruitment of activated myosin during Step 2, which is required for apicobasal shortening and invagination.

Design of a Tension-Based Mechanical Model for Ascidian Endoderm Invagination

Our experimental observations suggest that boundary-specific cortical tensions, set by levels of activated myosin, could be sufficient to cause the cell shape changes that drive ascidian invagination. To test this idea, and explore general design constraints on a cortical tension-based mechanism for ascidian invagination, we developed computer simulations that predict the dynamics of cell shape change given tension values for different boundaries. Then we randomly sought boundary-specific tension values for which the simulations reproduce shape changes we observed during Step 1 and Step 2.

Details of model construction and analysis are presented in Supplementary Modeling Procedures. In brief, we modeled a 2D frontal cross section of an ascidian embryo containing a small blastocoel. We considered only the two cell types—endoderm and mesectoderm (mesoderm plus ectoderm)—distinguished by our immunostaining of phosphomyosin. This implies seven distinct cell boundary types (Figure 5A): apical, lateral, and basal boundaries for endoderm and mesectoderm, plus the lateral endoderm-mesectoderm boundary. We represented each cell boundary as a connected set of smaller elements (Figure 5A), and we endowed these elements with two key mechanical properties designed to mimic those of a cortical actomyosin network: active contractility, characterized by a fixed tension T; and passive resistance to deformation, characterized by an effective internal viscosity μ_{eff}. For simplicity, we set μ_{eff} to a fixed value for all boundaries and all simulations; relaxing this assumption had little or no effect on the overall results (see Figures S4C and S4D). In contrast, we allowed the tension T to vary for each of the seven boundary types. We assumed that the cytoplasm of all cells was effectively incompressible.

To compare simulated to measured shape changes, we designed initial embryo geometries to match frontal cross-sections of mid 64-cell (pre-Step 1) or early 112-cell (pre-Step 2) embryos (Figure 5B). We used an independent starting geometry for Step 2 rather than simply continuing successful Step 1 simulations (with Step 2-specific parameters), because the ectoderm cleavage that occurs between Steps 1 and 2 (Figure 1A) creates smaller and more cuboidal ectoderm cells. Then we used quantitative geometric descriptors of cell and embryo shape to define target geometries for simulations to

match after a fixed time (Figures 5B and 5C, 30 simulated minutes for Step 1; 24 simulated minutes for Step 2). For Step 1, target criteria specified an endoderm plate that was tall, apically flat and narrow, and broad basally. For Step 2, target criteria specified a sufficiently deep invagination while maintaining constricted apices and an apically smooth mesectoderm. For both steps, we also required that there is no excessive apical or basal cell bulging. Movie S6 and Movie S7 show successful examples of Step 1 and 2 simulations.

Some simple considerations simplified our random parameter space searches: First we assumed that the tension on the lateral endoderm-mesectoderm boundary was the average of lateral mesectoderm and lateral endoderm tensions. Second, in initial simulations, we found that to reproduce blastocoel shapes correctly, basal tensions must be similar to lateral tensions for each cell type (Figure S4G), consistent with the similar levels of activated myosin we measured on lateral and basal endoderm surfaces (Figures 3D–3F). Therefore, we constrained basal tensions to match lateral tensions for each cell. Relaxing this assumption had little overall effect on the outcomes of our parameter space searches (Figures S4E and S4F). Finally, we constrained the maximum of the remaining four tensions to a fixed value to insure that cell shape changes unfold at similar rates for different parameter sets, and we scaled this fixed value so that simulated cell shapes approached steady state at a rate that is commensurate with what we observe in live embryos (see Figures 2A and 2B). With these assumptions/constraints, the outcomes of our simulations are determined by only three tension ratios whose values we could sample independently: the ratio of apical endoderm and mesectoderm tensions (Apical_E/M) and the ratios of lateral and apical tensions for each cell type (Endo_L/A and Mesecto_L/A)). Figures 5D and 5E show how varying these tension ratios affects the cell and embryo shapes attained from starting geometries for Steps 1 and 2. Intuitively, the L/A ratios tune apico-basal cell height, whereas Apical_E/M controls a tug-of-war between endoderm and mesectoderm for apical surface area.

Computer Simulations Support a Two-Step Mechanism for Invagination

Figures 5F and 5G show the distribution of parameter sets for which simulations satisfied either Step 1 (light and dark blue points) or Step 2 (red points) criteria. Figures S4A and S4B shows the same data plotted as tension values rather than ratios. For each step, successful parameter sets were clustered within well-defined regions. Moreover, successful regions for Step 1 and Step 2 did not overlap, strongly supporting the hypothesis that ascidian invagination involves two mechanistically distinct steps.

For all Step 1 solutions, the ratio of lateral to apical endoderm tension was low (Endo_L/A $<<$ 1), consistent with higher levels of active myosin at the apical surfaces of endoderm cells (Figures 3D and 3E). For most Step 1 solutions (dark blue points in Figures 5F and 5G), Apical_E/M values were significantly greater than 1, again consistent with observed phosphomyosin distributions. For those solutions in which Apical_E/M $<$ 1 (apical tension higher in the mesectoderm than the endoderm; light blue in Figures 5F and 5G), the ratio of lateral to apical mesectoderm tensions (Mesecto_L/A) was high enough to cause substantial flattening and spreading of mesectoderm (active epiboly). Moreover, we observed an inverse relationship between Mesecto_L/A and Apical_E/M across all Step 1 solutions (Figure 5G), suggesting that in principle either apical endoderm contraction or mesectoderm epiboly could account for the observed shape changes during Step 1 and that their effects are additive. To assess which of these mechanisms dominates in real embryos, we asked for which parameter sets simulations could also reproduce the cleavage-arrest effect of nocodazole treatment in which embryos invaginate with kinematics almost identical to controls but with fewer, larger mesectoderm cells (Figure S5A). Only a subset of the Step 1 solutions could reproduce both control and nocodazole-like geometries during Step 1, and all of these solutions had Apical_E/M values above 1.5 (Figures S5B and S5C). Combined with the phosphomyosin distribution, this analysis suggests that Step 1 in live embryos relies on high endoderm apical tensions, rather than on active mesectoderm epiboly.

For all successful Step 2 solutions, boundary tension values were consistent with observed patterns of active myosin accumulation (Figures 5F and 5G; red points): both apical and lateral endoderm tension were significantly higher than all other tensions (Figures S4A and S4B), and their ratio was tightly constrained (Figure 5F; 0.6 $<$ Endo_L/A $<$ 1.2), whereas Mesecto_LA ranged widely (red points in Figure 5G). Interestingly, parameters for which simulations mimicked the effects of nocodazole treatments overlapped with a large fraction of the wild-type solutions (yellow points in Figures S5B and S5C), suggesting that the Step 2 mechanism we identified is robust to variations in cell size and embryo geometry.

Simulations Reproduce the Effects of Myosin Inhibition by Blebbistatin and Y-27632

To further test our model, we asked whether it could reproduce the experimental effects of myosin inhibition by Blebbistatin and Y-27632. To simulate Blebbistatin treatment, we reduced cortical tensions on all cell surfaces to a fixed value T_B, representing a small and nonspecific residual tension, expressed as a percentage of the maximum value allowed in control simulations. Then we sampled values for T_B between 5% and 15%, comparing simulated morphologies to those measured for control or Blebbistatin-treated embryos. Indeed, predicted morphologies closely matched observed morphologies for both Step 1 and Step 2 (Figures S5D–S5G).

To simulate Rho/Rho-kinase inhibition, we chose subsets of the successful Step 1 and Step 2 parameter sets that represented ascidian-like invaginations (points colored dark blue and red in Figures 5F and 5G). For those parameters, we selectively reduced endoderm boundary tensions to percentages of their "control" values (different for each reference parameter set) to mimic the observed reduction of phosphomyosin staining in endoderm precursors of Y-treated embryos (Figures S5H–S5K). Then we compared the resulting simulated geometries to those observed in Y-treated embryos. During Step 1, Y treatment strongly reduces apical 1P-myosin staining (Figures 4I and 4J); indeed, reduction of apical endoderm tensions in our simulations reproduced most aspects of Step 1 morphologies in Y-treated embryos. However, simulations matched the slight increase in endoderm apicobasal height in embryos treated with Y in Step 1 only when we additionally reduced lateral endoderm tension. These results suggest that the 1P myosin observed at low levels on lateral endoderm cell surfaces during Step 1 produces active tension that contributes to apical flattening during Step 1 and is RhoA dependent. Unfortunately, the levels of 1P-myosin on lateral surfaces of Step 1 wild-type embryos were too low to reliably quantify their reduction in fixed Y-treated embryos (Figure 4S). During Step 2, lateral 1P-myosin levels are not affected by Y treatment

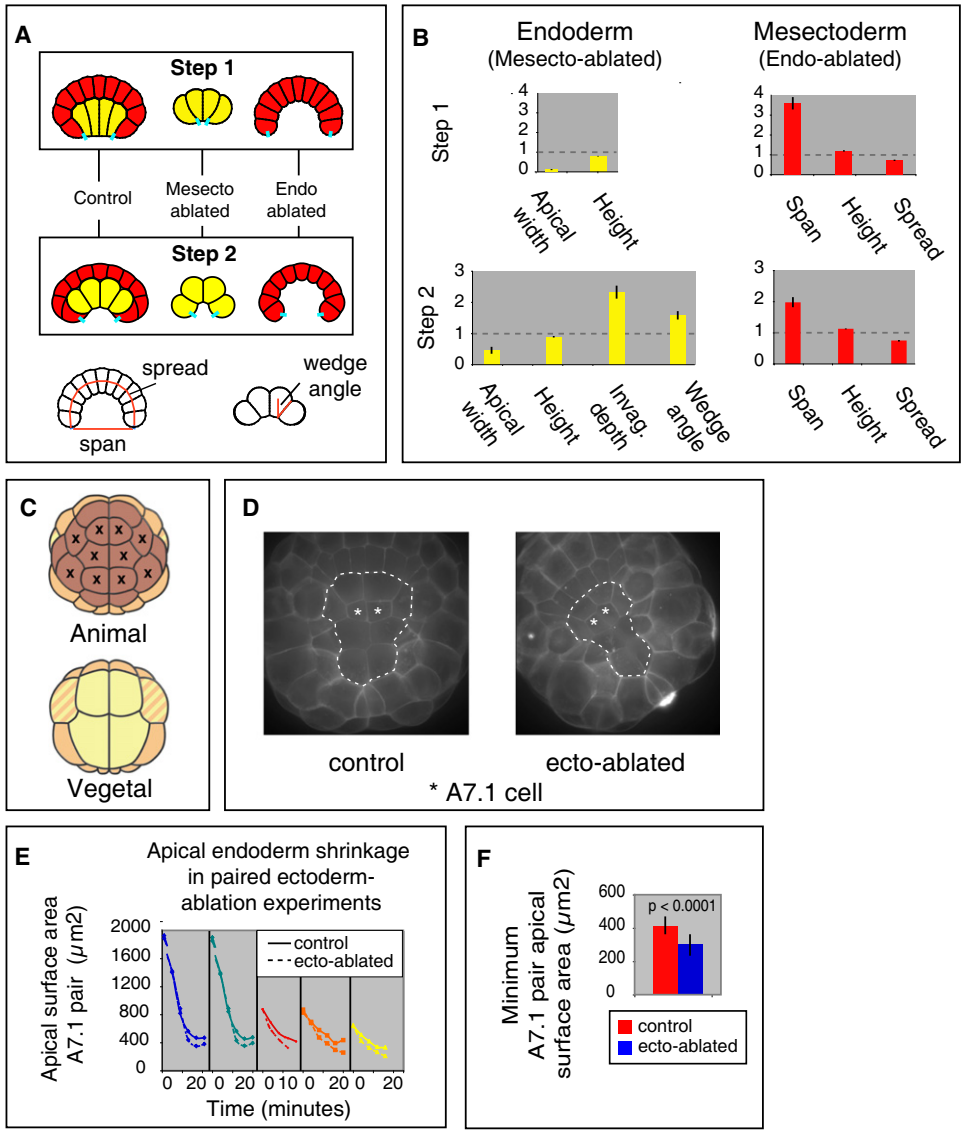

Figure 6. Effect on Invagination of Virtual and Experimental Ablations of Endoderm or Mesectoderm

(A) Schematic overview of the results of virtual ablations of mesectoderm and endoderm. The cyan segments indicate reference points used for measurements in (B). The bottom diagrams show how endoderm wedge angle, mesectoderm spread, and mesectoderm span were measured.

(B) Quantification of morphological changes produced by simulated ablation of mesectoderm or endoderm during Step 1 or 2. The height of each bar represents the fractional change for the indicated morphological measure, relative to controls, averaged over 100 runs with different passing parameters. Error bars are standard deviations. Cell height, apical width, and invagination depth were measured as in Figure 5B.

(C) Schematic view of a 32-cell embryo indicating the 10 laser-ablated ectoderm cells.

(D) Vegetal views of paired control (left) and ectoderm-ablated (right) embryos at late Step 1. Dashed lines mark the endoderm boundary (see Movie S1 for the corresponding time-lapse sequence).

(E) Changes in apical A7.1 surface area during Step 1 for five separate pairs of control versus ectoderm-ablated embryos.

(F) Minimum apical endoderm surface area achieved during Step 1 in control and ectoderm-ablated embryos. Figure S5 shows additional comparisons of model simulations with experimental perturbations (cleavage arrest by nocodazole, Rho kinase inhibition by Y-27632, and myosin inhibition by blebbistatin).

(Figures 4M–4P and 4S). Consistent with this, we found that reducing apical endoderm tension alone produced simulated morphologies that closely matched those measured for Y-treated embryos during Step 2.

The very good fit between our experimental observations and the simulations suggests that the dynamic spatio-temporal control of myosin-driven cortical tensions we identified is a major driver for ascidian invagination (summarized schematically in Figure 7). Importantly, neither apical contraction of the endoderm alone nor its apico-basal shortening alone can explain ascidian invagination; only a balance of the two can do so.

Mesectoderm Resists Endoderm Shape Changes during Steps 1 and 2

To gain further insights into how the interaction between endoderm and mesectoderm might contribute to cell shape changes during Steps 1 and 2, we simulated tissue ablation and asked how the nonablated tissue deformed relative to control embryos (Figure 6A). Starting with successful

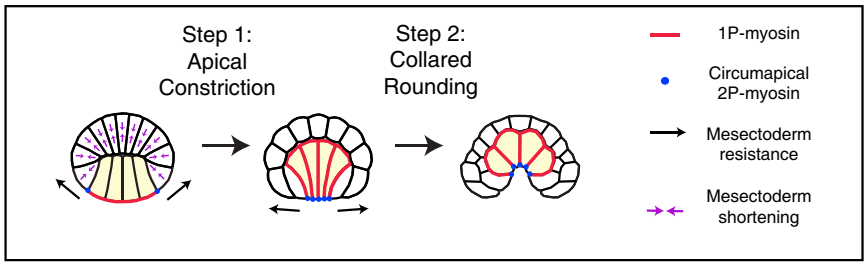

Figure 7. Model for a Two-Step Invagination of Ascidian Endoderm

Red, 1P-myosin; blue dots, 2P-myosin. Black arrows in Step 1 indicate mesectoderm resistance. Magenta arrows indicate apicobasal shortening and lateral spreading of mesectoderm (mechanism unknown), which may lower mesectoderm resistance.

ascidian-like parameter sets for Step 1 (dark blue in Figures 5F and 5G; Apical_EM > 1) or Step 2 (red in Figures 5F and 5G), we set all tension values associated with a given tissue to zero, thereby nullifying its mechanical contribution while maintaining appropriate apical, basal, and lateral identity in the remaining cells.

For successful Step 2 solutions, simulating endoderm ablation caused an increase in mesectoderm span and a slight reduction in its spread relative to control simulations (Figure 6B, bottom right; dotted lines show control measures). Simulating mesectoderm ablation produced a 2-fold increase in apical constriction and in the depth of endoderm invagination, without affecting endoderm cell height (Figure 6B, bottom left). These results support the hypothesis that endoderm-intrinsic forces are the major drivers for invagination and that mesectoderm opposes apical constriction, thereby resisting invagination.

When we simulated mesectoderm ablation during Step 1, the endoderm cells hyperconstricted their apices and slightly shortened apico-basally relative to controls (Figure 6B, upper left). Conversely, for simulated endoderm ablations during Step 1, the mesectoderm span increased, and its lateral spread was reduced (Figure 6B, upper right). Thus for tension parameter values that reproduce Step 1, the mesectoderm does not push against endoderm as it flattens and spreads. Instead, our simulations suggest that the mesectoderm resists apical endoderm constriction and that endoderm cells must generate sufficient force to overcome this resistance.

These results predict that ablating mesectoderm in live embryos should lead to an increase in apical endoderm constriction during Step 1. To test this experimentally, we laser ablated the 10 animal-most ectoderm cells at the late 32-cell stage (Figure 6C), then monitored apical endoderm shrinkage during Step 1 relative to paired controls (Figures 6D–6F; Movie S8). In 5/5 experiments, we observed an increase in the degree of apical endoderm constriction relative to the paired controls (minimum surface area = 299 ± 64 μm^2 in ablated embryos versus 413 ± 55 μm^2 in controls; $p < 0.0001$; $n = 5$), confirming the prediction that mesectoderm normally resists apical constriction during Step 1.

Discussion

A fundamental goal for studies of morphogenesis is to understand how embryonic cells organize force generation in space and time to produce characteristic patterns of tissue deformation. The work we present here suggests how spatiotemporal patterns of myosin activation could control cortical tensions to orchestrate the dynamics of ascidian endoderm invagination. First, our reconstructions identify a sequence of cell shape changes, conserved in four ascidian species, in which apical shrinkage and flattening of a columnar endoderm plate plus mesectoderm epiboly (Step 1) precede rapid basolateral shortening around tightly maintained apices (Step 2). Second, analysis of phospho-myosin distributions reveals spatiotemporal patterns of active myosin accumulation, consistent with the hypothesis that differential contractility drives cell shape changes during both steps. Third, our computer simulations show that distributions of cortical tension consistent with the phospho-myosin patterns we observe can reproduce the kinematics of invagination observed in normal and experimentally manipulated embryos. Tension parameter sets that reproduce Steps 1 and 2 occupy distinct, and widely separated, regions of parameter space, strongly supporting the idea that each step involves a unique distribution of boundary-specific tensions. Although we cannot rule out that additional force-generating mechanisms are involved, our results suggest that differential contractility plays a major role in shaping these boundary-specific tensions.

The systematic exploration of parameter space suggests that the basic mechanism for ascidian invagination is robust with respect to variation in tension parameter values. We observed only minor quantitative variations in otherwise similar patterns of cell shape change across four different species, and these variations can be mimicked in our simulations by small shifts in tension (data not shown). The finding that gastrulation proceeds normally in cleavage-arrested embryos and that simulations can reproduce both control and cleavage-arrested morphologies for the same choices of tension parameters further attest to this robustness.

Our simulation results suggest that in principle either apical endoderm constriction or active mesectoderm epiboly (or both) could drive endoderm deformation during Step 1. However, only active apical constriction of the endoderm is directly consistent with our 1P-myosin staining and can simultaneously explain the shape changes observed both in normal and in cleavage-arrested embryos. Furthermore, simulated ablations predict—and experimental ablations confirm—that mesectoderm epiboly does not contribute by active pushing, as is often assumed. Instead, contractile forces produced within the endoderm drive both steps of invagination, and mesectoderm resists endoderm shape change—in particular apical constriction—during both steps.

Both our data and simulations suggest that invagination itself involves the endoderm-intrinsic combination of apico-basal shortening and circumapical contraction—which we call collared rounding (Figure 7). Indeed, our simulations suggest that the apposition of strong basolateral and circumapical tension is the only way to reproduce an ascidian-specific invagination based on differential cortical tension. Importantly, inhibiting Rho/Rho kinase during Step 2 in vivo causes excessive apical expansion and reduced invagination without reducing apico-basal shortening, supporting the idea that apico-basal shortening produces invagination only when apical expansion is prevented by sufficient circumapical tension.

Two-phase invagination, with apical constriction and columnarization followed by apico-basal shortening, has been observed during invagination in other systems (see [15] for an excellent review). However, a role for myosin-dependent basolateral contraction in driving invagination, and the requirement for a balance between circumapical and basolateral tension, have not previously been documented. Apico-basal shortening is not a universal feature of all invaginating cells (notable examples are bottle cells that form during early gastrulation in *Xenopus* and dorso-lateral hingepoint cells that form during neurulation in chick and mouse), and thus why it should accompany some cases of invagination and not others remains an interesting puzzle. Perhaps the use of apico-basal shortening coupled to apical/circumapical contraction represents a specialization for rapid invagination as occurs, e.g., in ascidians and *Drosophila*. Alternatively, these differences may reflect the nature and relative contributions of forces acting intrinsic and extrinsic to the invaginating tissues—for example, the extent to which surrounding tissues resist invagination as shown here, or aid it, as in *Xenopus* gastrulation and vertebrate neurulation (reviewed in [15, 28]).

How are spatiotemporal patterns of myosin activation controlled within the endoderm lineage? As in other systems, we find that apical myosin accumulation plus constriction, and circumapical myosin accumulation plus maintenance of tight apices, depend on the Rho/Rho kinase pathway [9, 12, 29, 30]. The signaling pathways that control Rho during different invaginations are surprisingly diverse, alternately involving folded gastrulation, DPP, Hedgehog, EGF/ERK, Wnts, and ephrin receptors [30–35]. In *Ciona*, genome-scale ISH surveys identify a small set of candidate signaling molecules, some of which act in pathways that regulate Rho in other systems, and transcription factors that are expressed in a manner consistent with a role in Step 1 [36–38].

The pathways that control Rho-independent basolateral myosin recruitment during Step 2 remain unknown. Key candidates for proximal regulators are protein kinases known to phosphorylate myosin regulatory light chains in other contexts, including Myosin Regulatory Light Chain Kinase (MLCK), Myotonia Dystrophy-related Kinase (MRCK), and P-21 activated Kinase (PAK). Indeed, MLCK has been recently shown to control basal myosin activation during otic placode invagination [39]. Our efforts to test these candidate kinases with morpholino-based knockdowns and pharmacological interventions have so far yielded inconclusive results, but this remains an important goal for future studies.

Also unclear is what controls the transition from Step 1 to Step 2. Two-step control during gastrulation might be imposed by cell cycle progression, because Steps 1 and 2 coincide roughly with interphase and M-phase, respectively (K.S., unpublished data). A similar situation is found during polarization of the *C. elegans* zygote, where cell cycle progression from interphase to M-phase controls a transition between distinct modes of control over myosin activity (E.M. et al., unpublished). Alternatively, the transition from Step 1 to Step 2 could reflect the temporal dynamics of transcriptional regulation within the endoderm lineage. Indeed, transcriptional profiles in vegetal cells evolve quickly between the mid 64- and the late 112-cell stage, and a small number of secreted factors, including EphrinAc and BMP3, and transcription factors such as Ihx3 or TTF1 are expressed specifically in all invaginating cells during the 112-cell stage.

In summary, our results identify spatiotemporal control over myosin activity as a key physiological intermediate between the gene regulatory networks that control endoderm-specific differentiation and the mechanics of cell shape change that drive endoderm invagination. Future studies combining perturbations of key regulatory factors with the analysis of cytoskeletal dynamics and cell shape change in this simple embryo will provide a unique window into the mechanisms that integrate tissue morphogenesis with a global developmental program.

Experimental Procedures

Embryo Culture and Treatments

Embryos of *Ciona intestinalis*, *Phallusia mammillata, Ciona savignyi*, and *Boltenia villosa* were obtained and cultured as previously described [19, 40, 41]. We treated embryos in seawater with 1.3 μM nocodazole, 1 μM cytochalasin, 100 μm blebbistatin, or 100 μM Y-27632 (Sigma), at the 64- or early 112-cell stage.

3D Reconstructions and Morphometric Analysis

Phalloidin-stained embryos were prepared and imaged as described [19]. For recontructions of live *Phallusia* embryos, we imaged embryos in artificial seawater containing FM4-64 (5 mg/ml, Molecular probes), via a two-photon confocal microscope (LSM510 NLO microscope) with a 63× objective (C-Apochromat 1.2 W-corr, Carl Zeiss, Inc.) and 1020 nm illumination. For each embryo/time point, we collected a complete z-series at 3 μm intervals. Raw confocal stacks are available for download at http://crfb.univ-mrs.fr/aniseed/embryo-collection.php.

We performed morphometric measurements with the 3D Virtual Embryo software [19]. We calculated changes in mean apical surface area for a given cell as a ratio of the final over initial value ($n \geq 3$ for each stage). We defined the total shape deformation for a given cell between two stages as the sum over all unit-less normalized shape descriptors (sphericity, elongation, flatness, squareness, entropy, surface/volume, convexity) of the absolute value of the difference between initial and final values measured for that descriptor.

Immunostaining and Quantitative Analysis of Phosphomyosin Distributions

We fixed embryos for 30 min in 100 mM HEPES [pH 7.0], 100 mM EGTA, 10 mM $MgSO_4$, 2% formaldehyde, 0.1% gluteraldehyde, 300 mM dextrose, and 0.2% Triton-X. We treated embryos for 20 min in 0.1% sodium borohydride in PBS to reduce unreacted aldehydes, then incubated 24 hr at room temperature with primary antibodies to ser19 phospho-myosin (1:250, Cell Signaling) or thr18/Ser19 phospho-myosin (1:500, Cell Signaling), rinsed three times, then incubated 24 hr in secondary goat anti-rabbit Alexa Fluor 488 or 568 nm (1/600, Invitrogen) and Bodipy FL 488 nm or Alexa 568 nm phallacidin (1:200, Invitrogen). We mounted embryos in Murray's Clear and confocal imaged them as described previously [42].

We measured fluorescence intensities along cell boundaries in ImageJ (http://rsbweb.nih.gov/ij/) as mean gray levels averaged over 1 μm thick lines drawn along the boundary of interest. We measured apical 1P-myosin from single cross-sections produced by reslicing raw image stacks parallel to the animal-vegetal (AV) axis, and lateral 1P-myosin from single confocal sections taken perpendicular to the AV axis. We measured circumapical 1P- and 2P-myosin from maximum intensity projections of the apical surface. We measured cytoplasmic background levels for each cell as the mean gray level within a small (5 μm^2) box located within the deep cytoplasm.

GFP Fusions and Dominant-Negative Constructs

We constructed a Gateway compatible Ci-ZO-1 clone by PCR-amplifying the coding sequence from a cDNA clone (Cicl035p23, gift of Yutaka Satou and Nori Satoh) flanked by gateway compatible attR1-attR2 sequences (forward primer: 5′GGGGACAAGTTTGTACAAAAAAGCAGGCTCAGAAAAAATGATGGATGAGCTAATATGGCAGGAGC3′, reverse primer: 5′GGGGACCACTTTGTACAAGAAAGCTGGGTTGAAATGGTCGATAAGAACAGAAACGC3′). We recombined this fragment into a p221-DONR [43]. A Gateway-compatible RhoA dominant-negative construct T19N [44] was generated by point mutation. Constructs were recombined in pSPE3-RfA-Venus and pSPE3-RfA, respectively [43], for RNA synthesis.

Laser Ablations

Animal cells of 32-cell stage embryos (see Figure 7C) were ablated with a Micropoint nitrogen-pumped dye laser (Photonics Instruments, 365 nm, 10–20 hz, maximum power) mounted on a Nikon Eclipse TE2000-U microscope. A short (<1 s) laser pulse focused at the apical surface of a cell was sufficient for lysis. Lysed cells' remnants were removed manually from the embryos before imaging. Paired control and ablated embryos were labeled with the membrane dye FM4-64, then imaged with a DeltaVision microscope through a 40× water immersion lens. A stack of 15–20 sections spaced at 1 μm intervals were collected every 10 s. We then measured endoderm apical surface areas from maximal projections with ImageJ.

Computer Simulations and Searches of Tension Parameter Space

All simulations and analysis were performed with custom software. See Supplementary Modeling Procedures for details.

Supplemental Information

Supplemental Information includes Supplementary Modeling Procedures, five figures, and eight movies and can be found with this article online at doi:10.1016/j.cub.2010.06.075.

Acknowledgments

This work was supported by CNRS (P.L.), the Marine Genomics Europe FP6EU network of excellence (P.L.), and by NIGMS Center of Excellence grant P50 GM006605 (E.M.). F.R. was funded by the French ministry of research and higher education and by the Association pour la Recherche sur le Cancer (ARC); K.S. by an NIH-NRSA fellowship. We thank Garry Odell, Victoria Foe, and David McClay for comments on the manuscript. We also acknowledge the staff of the Marine biology Station of Roscoff for collecting animals in France and François Graziani (IBDML) for animal care.

Received: April 8, 2010
Revised: June 22, 2010
Accepted: June 30, 2010
Published online: August 5, 2010

References

1. Davidson, L.A., Koehl, M.A.R., Keller, R., and Oster, G.F. (1995). How do sea urchins invaginate? Using biomechanics to distinguish between mechanisms of primary invagination. Development *121*, 2005–2018.
2. Clausi, D.A., and Brodland, G.W. (1993). Mechanical evaluation of theories of neurulation using computer simulations. Development *118*, 1013–1023.
3. Jacobson, A.G., Oster, G.F., Odell, G.M., and Cheng, L.Y. (1986). Neurulation and the cortical tractor model for epithelial folding. J. Embryol. Exp. Morphol. *96*, 19–49.
4. Muñoz, J.J., Barrett, K., and Miodownik, M. (2007). A deformation gradient decomposition method for the analysis of the mechanics of morphogenesis. J. Biomech. *40*, 1372–1380.
5. Odell, G.M., Oster, G.F., Alberch, P., and Burnside, B. (1981). The mechanical basis of morphogenesis. I. Epithelial folding and invagination. Dev. Biol. *85*, 446–462.
6. Pouille, P.-A., and Farge, E. (2008). Hydrodynamic simulation of multicellular embryo invagination. Phys. Biol. *5*, 015005.
7. Brodu, V., and Cassanova, J. (2006). The RhoGAP *crossveinless-c* links *trachealess* and EGFR signaling to cell shape remodeling in *Drosophila* tracheal invagination. Genes Dev. *20*, 1817–1828.
8. Lee, J.-Y., and Harland, R.M. (2007). Actomyosin contractility and microtubules drive apical constriction in *Xenopus* bottle cells. Dev. Biol. *311*, 40–52.
9. Nikolaidou, K.K., and Barrett, K. (2004). A Rho GTPase signaling pathway is used reiteratively in epithelial folding and potentially selects the outcome of Rho activation. Curr. Biol. *14*, 1822–1826.
10. Simões, S., Denholm, B., Azevedo, D., Sotillos, S., Martin, P., Skaer, H., Hombría, J.C.-G., and Jacinto, A. (2006). Compartmentalisation of Rho regulators directs cell invagination during tissue morphogenesis. Development *133*, 4257–4267.
11. Young, P.E., Pesacreta, T.C., and Kiehart, D.P. (1991). Dynamic changes in the distribution of cytoplasmic myosin during *Drosophlia* embryogenesis. Development *111*, 1–14.
12. Beane, W.S., Gross, J.M., and McClay, D.R. (2006). RhoA regulates initiation of invagination, but not convergent extension, during sea urchin gastrulation. Dev. Biol. *292*, 213–225.
13. Dawes-Hoang, R.E., Parmar, K.M., Christiansen, A.E., Phelps, C.B., Brand, A.H., and Wieschaus, E. (2005). *folded gastrulation*, cell shape change, and the control of myosin localization. Development *132*, 4165–4176.
14. Ferreira, M.C., and Hilfer, S.R. (1993). Calcium regulation of neural fold formation: Visulation of the actin cytoskeleton in living chick embryos. Dev. Biol. *159*, 427–440.
15. Keller, R., Davidson, L.A., and Shook, D. (2003). How we are shaped: The biomechanics of gastrulation. Differentiation *71*, 171–205.
16. Pilot, F., and Lecuit, T. (2005). Compartmentalized morphogenesis in epithelia: From cell to tissue shape. Dev. Dyn. *232*, 685–694.
17. Leptin, M. (2005). Gastrulation movements: The logic and the nuts and bolts. Dev. Cell *8*, 305–320.
18. Munro, E., Robin, F., and Lemaire, P. (2006). Cellular morphogenesis in ascidians: How to shape a simple tadpole. Curr. Opin. Genet. Dev. *16*, 399–405.
19. Tassy, O., Daian, F., Hudson, C., Bertrand, V., and Lemaire, P. (2006). A quantitative approach to the study of cell shape changes and interactions during early chordate embryogenesis. Curr. Biol. *16*, 345–358.
20. Nishida, H. (1986). Cell division pattern during gastrulation of the ascidian, *Halocynthia roretzi*. Dev. Growth Differ. *28*, 191–201.
21. Satoh, N. (1978). Cellular morphology and architecture during early morphogenesis of the ascidian egg: An SEM study. Biol. Bull. *155*, 608–614.
22. Matsumura, F. (2005). Regulation of Myosin II during cytokinesis in higher eukaryotes. Trends Cell Biol. *15*, 371–377.
23. Komatsu, S., and Ikebe, M. (2004). ZIP kinase is responsible for the phosphorylation of myosin II and necessary for cell motility in mammalian fibroblasts. J. Cell Biol. *165*, 243–254.
24. Mizutani, T., Haga, H., Koyama, Y., Takahashi, M., and Kawabata, K. (2006). Diphosphorylation of the myosin regulatory light chain enhances the tension acting on stress fibers in fibroblasts. J. Cell. Physiol. *209*, 726–731.
25. Uchimura, T., Fumoto, K., Yamamoto, Y., Ueda, K., and Hosoya, H. (2002). Spatial localization of mono- and diphosphorylated myosin II regulatory light chain at the leading edge of motile HeLa cells. Cell Struct. Funct. *27*, 479–486.
26. Straight, A.F., Cheung, A., Limouze, J., Chen, I., Westwood, N.J., Sellars, J.R., and Mitchison, T.J. (2003). Dissecting temporal and spatial control of cytokinesis with a myosin II Inhibitor. Science *299*, 1743–1747.
27. Ishizaki, T., Uehata, M., Tamechika, I., Keel, J., Nonomura, K., Maekawa, M., and Narumiya, S. (2000). Pharmacological properties of Y-27632, a specific inhibitor of Rho-associated kinases. Mol. Pharmacol. *57*, 976–983.
28. Sai, X., and Ladher, R. (2008). FGF signaling regulates cytoskeletal remodeling during epithelil morpohogenesis. Curr. Biol. *18*, 976–981.
29. Barrett, K., and Leptin, M. (1997). The Rho GTPse and a putative RhoGEF mediate a signaling pathway for the cell shape changes in *Drosophila* gastrulation. Cell *91*, 905–915.
30. Kinoshita, N., Sasai, N., Misaki, K., and Yonemura, S. (2008). Apical accumulation of Rho in the neural plate is important for neural plate cell shape change and neural tube formation. Mol. Biol. Cell *19*, 2289–2299.
31. Corrigall, D., Walther, R.F., Rodriguez, L., Fichelson, P., and Pichaud, F. (2007). Hedgehog signaling is a principal inducer of Myosin-II-driven cell ingression in *Drosophila* epithelia. Dev. Cell *13*, 730–742.
32. Escudero, L.M., Bischoff, M., and Freeman, M. (2007). Myosin II regulates complex cellular arrangement and epithelial architecture in *Drosophila*. Dev. Cell *13*, 717–729.
33. Lee, J.-Y., Marston, D.J., Walston, T., Hardin, J., Halberstadt, A., and Goldstein, B. (2006). Wnt/frizzled signaling controls *C. elegans* gastrulation by activating acto-myosin contractility. Curr. Biol. *16*, 1986–1997.
34. Nishimura, M., Inoue, Y., and Hayashi, S. (2007). A wave of EGFR signaling determines cell alignment and intercalation in the *Drosophila* tracheal placode. Development *134*, 4273–4282.
35. Xu, N., Keung, B., and Myat, M.M. (2008). Rho GTPase controls invagination and cohesive migration of the *Drosophila* salivary gland through Crumbs and Rho-kinase. Dev. Biol. *321*, 88–100.
36. Imai, K.S., Hino, K., Yagi, K., Satoh, N., and Satou, Y. (2004). Gene expression profiles of transcription factors and signaling molecules in

the ascidian embryo: Towards a comprehensive understanding of gene networks. Development *131*, 4047–4058.

37. Miwata, K., Chiba, T., Horii, R., Yamada, L., Kubo, A., Miyamura, D., Satoh, N., and Satou, Y. (2006). Systematic analysis of embryonic expression profiles of zinc finger genes in *Ciona intestinalis*. Dev. Biol. *292*, 546–554.
38. Shi, W., and Levine, M. (2008). Ephrin signaling established asymmetric cell fates in an endomesoderm lineage of the *Ciona* embryo. Development *135*, 931–940.
39. Colas, J.F., and Schoenwolf, G.C. (2001). Towards a cellular and molecular understanding of neurulaiton. Dev. Dyn. *221*, 117–145.
40. McDougall, A., and Sardet, C. (1995). Function and characteristics of repetitive calcium waves associated with meiosis. Curr. Biol. *3*, 318–328.
41. Munro, E.M., and Odell, G.M. (2002). Polarized basolateral cell motility underlies invagination and convergent extension of the ascidian notochord. Development *129*, 13–24.
42. Foe, V.E., and von Dassow, G. (2008). Stable and dynamic microtubules coordinately shape the myosin activation zone during cytokinetic furrow formation. J. Cell Biol. *183*, 457–470.
43. Roure, A., Rothbächer, U., Robin, F., Kalmar, E., Ferone, G., Lamy, C., Missero, C., Mueller, F., and Lemaire, P. (2007). A multicassette Gateway vector set for high throughput and comparative analysis of ciona and vertebrate embryos. PLoS ONE *2*, e916.
44. Philips, A., Blein, M., Robert, A., Chambon, J.P., Baghdiguian, S., Weill, M., and Fort, P. (2003). Ascidians as a vertebrate-like model organism for physiological studies of Rho GTPase signaling. Biol. Cell *95*, 295–302.
45. Ueda, K., Murata-Hori, M., Tatsuka, M., and Hosoya, H. (2002). Rho kinase contributes to diphosphorylation of myosin II regulatory light chain in non muscle cells. Oncogene *21*, 5852–5860.

Current Biology, Volume *20*

Supplemental Information

Sequential Activation of Apical and Basolateral Contractility Drives Ascidian Endoderm Invagination

Kristin Sherrard, François Robin, Patrick Lemaire, and Edwin Munro

1) Supplementary modeling procedures

2) Supplementary references

3) Supplementary figures 1-5

SUPPLEMENTARY MODELING PROCEDURES

Overview. We model a cell in two dimensions as a collection of discrete elements, joined together to form a continuous boundary that surrounds an incompressible cytoplasm of volume V. Adjacent cells share elements along their common boundaries. We distinguish three fundamental boundary types: Apical boundaries face the outer medium; lateral boundaries are formed by two adjacent cells; and basal boundaries face an internal blastocoel (Figure A1). Along a boundary, elements are connected directly to one another at nodes, which serve as material points of reference. At points where 3 boundaries meet, elements are connected to a single common vertex by simple linear springs (Figure A2).

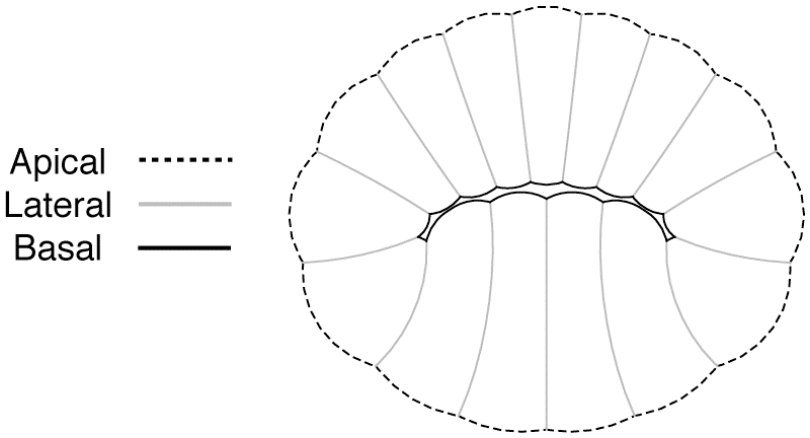

Figure A1. Architecture of a model embryo. (*A) Boundary types for polarized cells within a two-dimensional tissue. (B) architecture of a single cell boundary.*

Mechanical properties of cortical elements. We endow each boundary element with a tension T and an effective viscosity μ_{eff}. By assumption, the magnitude of T reflects the strength of actomyosin contractility, plus possible contributions from cell cortex/plasma membrane elasticity and cell-cell adhesion (Lecuit and Lenne 2007). We assume that the value of T is the same and constant in time for all elements within a given boundary, but different for different boundaries, and for the two phases of

invagination (see main text and below). The effective viscosity μ_{eff} represents the tendency of the cell cortex to creep or flow in response to externally applied forces, or gradients in cortical tension, on the timescale (minutes) over which cell shape changes occur (Bray and White, 1988, Bausch et al, 1999, Munro et al, 2004). For simplicity, we assign the same μ_{eff} to all elements, regardless of boundary type.

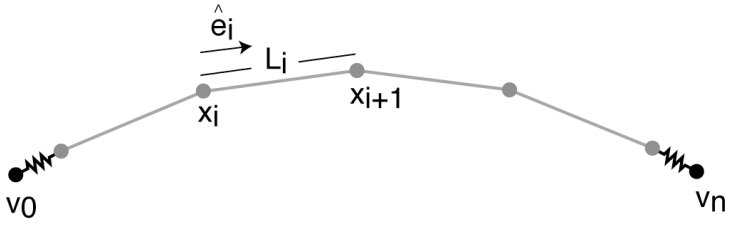

Figure A2. Model representation of a single cell boundary as a collection of interconnected elements.

With these assumptions, the force that a boundary element i exerts upon its neighbors at nodes i and i+1 is +/- $\vec{F}_{cortex}$ respectively, where

(1)
$$\vec{F}_{cortex} = \left[T + \frac{\mu_{eff}}{L_i} \frac{dL_i}{dt} \right] \hat{e}_i$$

$$= \left[T + \frac{\mu_{eff}}{L_i} ((x_{i+1} - x_i) * (\frac{dx_{i+1}}{dt} - \frac{dx_i}{dt}) + (y_{i+1} - y_i) * (\frac{dy_{i+1}}{dt} - \frac{dy_i}{dt})) \right] \hat{e}_i ,$$

where $\vec{x}_i = (x_i, y_i)$ are the coordinates of the ith node, L_i is the instantaneous length of element i, and $\hat{e}_i$ is a unit vector lying tangent to boundary element i and pointing towards node i+i (Figure A2).

Vertex Spring Forces. We connect the terminal cortical nodes of each boundary to a common vertex through simple linear springs:

(2) $$\vec{F}_{vertex} = k_s(\vec{v} - \vec{x}),$$

where k_s is the spring stiffness, $\vec{v}$ is the vertex position, and $\vec{x}$ is the position of a terminal cortical node. This construction reflects the implicit assumption that there is no flow of cortical material from one boundary to the other. This is likely to be true at the apical surface where adherens junctions are thought to anchor the apical contraction forces produced by neighboring cells (e.g. Costa et al, 1998, Dawes-Hoang et al, 2005)). Relaxing this assumption through more detailed representations of cell-cell adhesion has little effect on the dynamics of cell shape change and embryo deformation we describe here (Sherrard and Munro, unpublished).

Pressure and Contact Forces. Ignoring the small changes in volume that we measured during invagination (Figure S2E), we assume that each cell maintains a constant volume (represented by cross-sectional area in 2D), and that the internal cytoplasm is effectively incompressible. We enforce this assumption (approximately) by applying a pseudo-pressure force normal to each cortical segment:

(3) $$\vec{F}_{pressure} = \beta * L * \frac{A - A_0}{A_0} \hat{n} \quad ,$$

where A is current area, A_0 is the area setpoint, L is segment length, $\hat{n}$ is the unit outward normal to that segment, and β is a constant. In practice, we set β to the minimal value required to maintain cell volumes within 95% of the target. In some simulations, collective deformations would cause basal surfaces of cells to cross one another. To prevent this, we impose contact forces (Figure A3), equal and opposite on adjacent boundaries, which act normal to the average orientation of the two boundaries, at

the center of the zone of contact, and whose magnitude is proportional to the length of the zone of contact and the square of the average distance d between boundaries:

(4) $$\vec{F}_{contact} = +/- \; F_{rep} * L_C * (d - d_{min})^2 * \hat{n}_c$$

Where L_C is the length of the contact zone, and d_{min} is minimal allowable distance between boundaries, F_{rep} is the magnitude of the repulsive force, and $\hat{n}_c$ is the appropriate unit normal vector.

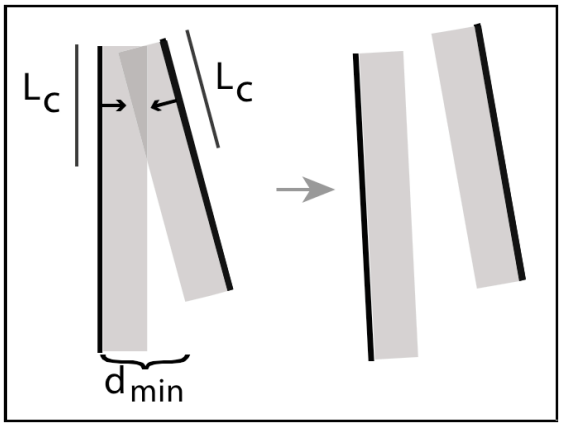

Figure A3. Action of contact forces.

Equations of motion. Neglecting inertial forces, which are small at cellular length scales (Howard, 2001), Newtons's Second Law implies that the sum of all forces acting on each node is ~0. Collecting (1) – (4), we have for all nodes along a single boundary.

(5) $$\vec{F}_{cortex,i} - \vec{F}_{cortex,i-1} + \vec{F}_{contact,i} + \vec{F}_{vertex,i} + \vec{F}_{pressure,i} - \mu_g \frac{\vec{x}_i}{dt} = 0,$$

$$i = 0, 1, \ldots, n,$$

The last term in (5) could be interpreted as the viscous resistance to motion of the cell surface relative to surrounding extracellular fluids. This contribution is likely to be small relative to the internal resistance

of the cell to deformation (e.g. Bausch et al, 1999). Without this term, however, the equations of motion are not well-posed because they are indifferent to rigid body translations of the boundary. In practice, we set the value of μ_g small enough that it contributes negligibly to the simulated dynamics (see below).

For each cell boundary, (5) represents a coupled system of ordinary differential equations:

$$(6) \qquad [A]\begin{pmatrix} \frac{dx_0}{dt} \\ \frac{dy_0}{dt} \\ . \\ . \\ . \\ \frac{dx_n}{dt} \\ \frac{dy_n}{dt} \end{pmatrix} + \begin{pmatrix} (\vec{F}_{contact,0})_x + (\vec{F}_{vertex,0})_x + (\vec{F}_{pressure,0})_x \\ (\vec{F}_{contact,0})_y + (\vec{F}_{vertex,0})_y + (\vec{F}_{pressure,0})_y \\ . \\ . \\ . \\ (\vec{F}_{contact,n})_x + (\vec{F}_{vertex,n})_x + (\vec{F}_{pressure,n})_x \\ (\vec{F}_{contact,n})_y + (\vec{F}_{vertex,n})_y + (\vec{F}_{pressure,n})_y \end{pmatrix} = 0 ,$$

where A is a matrix whose coefficients depend on μ_{eff}, μ_g, and the coordinates of the nodes. At each time step, we invert A using standard methods (Press et al, 1996), and then use the first order Euler method to approximate new positions for boundary nodes. Finally, at each time step, after updating node positions for all boundaries, we update the positions of connecting vertices by solving:

$$(7) \qquad \sum_i \vec{F}_{vertex,i} = k_s(\vec{v} - \vec{x}_i) = 0$$

Choosing values for parameters other than boundary-specific contractile tensions. A description of how we sampled parameters governing boundary-specific contractile tensions appears below. Table A1 lists all other parameters used in this study. Our kinematic observations in living embryos are consistent with an asymptotic approach to mechanical equilibrium during Step 1, followed by rapid cell shape change after the transition to Step 2 (Figure 2J,K and Supplemental Figure S2E). Likewise, in our simulations of Step 1, model embryos approach mechanical equilibrium at a rate that depends on the relative magnitudes of the maximum boundary tension and the effective viscosity (data not shown). Thus, to ensure a meaningful comparison between our simulations and the measured kinematics: First, we scaled all forces relative to a maximum tension value of 1. We chose a duration for Step 1 simulations $t_{step1} = \sim 30$ minutes to match the duration of Step 1 in *Ciona intestinalis* embryos. Then we chose a value for μ_{eff} such that on average simulated embryos reach a similar point in their approach to equilibrium as real embryos near the end of Step 1 (determined by comparing plots of average apical endoderm width vs time for simulations vs live embryos; data not shown). Then we chose the duration for Step 2 simulations t_{step2} such that the ratio of simulations times $\frac{t_{step1}}{t_{step2}}$ matched the relative durations of Step 1 and Step 2 in *Ciona intestinalis* embryos. For parameters governing cytoplasmic pressure, cell-cell repulsion, and linkage of boundary segments to tri-cell vertices, we assigned minimal values required to keep departures from target cell volumes, gaps between cells and gaps between adjacent boundary segments within acceptable levels (see Table A1). Using larger values for these parameters did not significantly change simulated dynamics, but increased the tendency towards numerical instability. Finally, by comparing simulation outcomes for decreasing values of μ_g (relative to fixed μ_{eff}), we determined a value for μ_g that was large enough to allow efficient numerical solution of the equations of motion, but small enough that it did not significantly affect the simulated dynamics.

Sampling boundary-specific tension parameter space. We assigned distinct cortical tension values to each of the 7 boundary types: apical endoderm (T_{Endo_Apical}), apical mesectoderm ($T_{Mesecto\_Apical}$), lateral endoderm-endoderm ($T_{Endo\_Lateral}$), lateral mesectoderm-mesectoderm ($T_{Mesecto\_Lateral}$), lateral endoderm-mesectoderm ($T_{Endo\_Mesecto}$), basal endoderm (T_{Endo_Basal}), and basal mesectoderm ($T_{Mesecto\_Basal}$). We constrained the tension along endoderm-mesectoderm boundaries to be the average:

$$T_{Endo\_Mesecto} = \frac{T_{Endo\_Lateral} + T_{Mesecto\_Lateral}}{2} \quad (8)$$

In initial simulations, we allowed basal tensions to vary between the absolute max and min values allowed for all tension values, and found that these tensions were strongly constrained to be close to 0.5 their cells' respective lateral tensions for passing runs (Figure S4G). Thus for subsequent analysis, we constrained basal tensions to be one half the corresponding lateral tensions. Note that the distributions of basal and lateral phosphomyosin in fixed embryos are consistent with these assumptions (Figure 4) and the fact that basal boundaries represent a single cell boundary while lateral boundaries represent the summed contributions of two adjacent cells.

We allowed the remaining 4 tension values to vary freely. For reasons explained in the main text, we focus on three dimensionless tension ratios:

$$mesecto_{LA} = \frac{T_{Mesecto\_Lateral}}{T_{Mesecto\_Apical}},\ endo_{LA} = \frac{T_{Endo\_Lateral}}{T_{Endo\_Apical}},\ \text{and}\ apical_{EM} = \frac{T_{Endo\_Apical}}{T_{Mesecto\_Apical}} \quad (9)$$

We devised a simple method to sample these tension ratios uniformly within the 3-dimensional cube defined by

(10) $$0.05 < endo_{LA} < 5; \quad 0.05 < mesecto_{LA} < 5; \quad 0.2 < apical_{EM} < 5 .$$

Briefly, we sampled each tension ratio randomly and independently from its overall range to insure uniform sampling of the cube. Each random choice of three ratios imply relative values for all four tensions, and imply which of the four is maximal. We scaled all four tensions to make the maximum tension identically 1. With this scheme, the individual tension values varied as follows: $0.01 < T_{Endo\_Lateral} < 1; 0.01 < T_{Mesecto\_Lateral} < 1;\ 0.04 < T_{Endo\_Apical} < 1; 0.04 < T_{Mesecto\_Apical} < 1$. We searched a minimum of 64,000 parameter sets, equivalent (in terms of number of samples) to sampling a mesh of at least > 40 evenly spaced points for each of three tension ratios. Because all conditions other than starting geometry were held constant, hit rates are comparable for Step 1 and Step 2 searches and were 0.17% for Step 1 and 0.07% for Step 2.

Spatial discretization of cell boundaries. We chose an optimal average segment length L asymptotically, i.e. by progressively decreasing lengths in repeated test simulations until the simulated dynamics no longer changed significantly. Because the lengths of cortical segments change as simulations proceed, it was necessary to rediscretize cell boundaries locally when segment lengths increase or decrease too far: when segment's lengths exceeded $L_{\max}$, we replaced them with a pair of smaller segments of identical length; when segment's lengths fell below $L_{\min}$, we deleted the segment, extending the ends of adjacent segments to the midpoint of the deleted segment. In practice, we found

that basal cell boundaries required finer discretization than lateral or apical cell boundaries to properly resolve cell-cell interactions across the blastocoel space (see Table A1 for values).

Table A1. Summary of key parameter values.

Parameter	Symbol	Value	Criteria for setting value
Maximal tension	T_{max}	1	Arbitrary, but fixed reference value
Step 1 run time	t_{step1}	30 minutes	Set to match duration of Step 1 in *Ciona intestinalis*
Step 2 run time	t_{step2}	24 minutes	Set to match duration of Step 2 in *Ciona intestinalis*
Effective viscosity	μ_{eff}	0.5*sec	Chosen so that average passing runs are at similar position in approach to mechanical equilibrium as real embryos at the end of Step 1.
Boundary friction	μ_g	0.0017*sec/μm^2	Determined asymptotically
Repulsive force multiplier	F_{rep}	0.05	Large enough to prevent boundary overlap
Pressure force multiplier	β	0.1	Large enough to maintain $(A-A_0)/A_0 < 0.05$

Vertex spring constant	k_s	1.6	sufficient to maintain gaps between vertex and boundaries < 0.5
Maximum segment length for apical and lateral boundaries	L_{max}	7 μm	Length below which simulation dynamics cease to change appreciably.
Minimum segment length for apical and lateral boundaries	L_{min}	3 μm	Set low enough relative to L_{max} to prevent cycles of segment insertion/removal
Maximum basal segment length	B_{max}	3 μm	Set low enough that asymmetries due to poor fit of basal cell regions around blastocoel did not significantly affect simulated dynamics.
Minimum basal segment length	B_{min}	1 μm	Set low enough relative to B_{max} to prevent cycles of segment insertion/removal
Integration timestep	t_{step}	0.06	Set to maximum value that avoids numerical instability.

Choosing starting geometries. The starting geometries for Step 1 and 2 shown in Figure 5 were derived from frontal views of fixed and reconstructed *Ciona* embryos at the appropriate stages (see Figure 1B).

A typical cross-section of an early gastrulation-stage *Ciona* embryo (Figure 1) comprises two rows of cells with four larger endoderm cells, two flanking mesodermal cells, and eight ectoderm cells (10 after the mid-invagination cleavage). The blastocoel is small but detectable in all embryos and the bases of cells rest within troughs created by junctions of cell bases on the opposite side of the blastocoel. Therefore our simulation's basic geometry was a row of 4 endoderm cells flanked on each side by a mesoderm cell (hereafter referred to as mesectoderm), and an overlying row of nine ectoderm cells, in order to specify a left-right symmetrical embryo with endoderm and mesectoderm cell bases offset by half a cell-diameter as observed in real embryos.

For each step, total cross-sectional area of the ectoderm, mesoderm, and endoderm cells at either the start of Step 1 or Step 2 was evenly distributed across the nine, two, and four cells of each type (i.e., mesoderm cells behaved like ectoderm in terms of their cortical tensions, but were slightly larger). Starting geometriess closely matched embryo aspect ratio (animal-vegetal length vs. left-right length), aspect ratio of each cell type (with slight modification to accommodate the extra ectoderm cell in Step 1 and the missing ectoderm cell in Step 2), and apical curvature animally and vegetally.

Robustness of simulation results with respect to implementation of the simulations. In early tests, we verified for individual simulations that the outcomes were insensitive to quantitative variation values of parameters governing spatial discretization of cell boundaries, steric, volumetric or connectivity constraints on cells, or the numerical integration of model equations, about the values we chose (see Table A1). We also found that the outcomes of Step 1 and Step 2 parameter searches were largely insensitive to minor variations in embryo geometry (including replacing the blastocoel by a single basal junction shared among endoderm and mesectoderm cells), the durations of Step 1 and Step 2 simulations, and the criteria used to determine passing Step 1 and Step 2 solutions. By insensitive, we

mean that the distributions of “successful” parameters were affected in minor ways, none of which had any impact on the conclusions presented here (data not shown).

2D vs 3D simulations. Using a 2D model to represent a 3D morphogenetic process raises a number of issues, which we discuss below. We start by emphasizing that the essential results provided by our 2D simulations are qualitative, expressible in sentences like: "A balance of apical and basolateral contraction is absolutely required for a deep invagination during Step 2." or "Distinct sets of cell-cell boundary tensions must govern cell shape change Step 1 and Step 2." or " The mesectoderm resists apical endoderm constriction - i.e. it pulls rather than pushes - during Step 1." The significance of these results does not depend on knowing the exact values of e.g. boundary-specific tensions. It is certain that quantitative details of model predictions – i.e. the exact set of points in tension parameter space for which the model simulations reproduce observed patterns of cell shape change - will depend on difference between 2D and 3D mechanics. The issue is whether the qualitative results do.

To a good first approximation, the invaginating ascidian embryo is rotationally symmetric. This means that qualitatively, the same balance of apical, lateral and basal tensions upon which our results depend operate within any lateral cross section through the embryo taken perpendicular to the plane of the sheet and passing through its center. Given this, we expect the main differences between 2D and 3D model predictions to come from three sources: (1) The use of 2D cross-sectional area as a proxy for 3D cell volume; (2) the contributions of out-of-plane forces, which we neglect in our 2D simulations, and (3) departures of cell and embryo geometries from rotational symmetry. Given the robustness of model predictions to variations in 2D geometry and other types of quantitative variation (see above), we do not expect (3) to affect our conclusions. We address the other 2 concerns below:

Use of 2D cross-sectional area as a proxy for 3D cell volume. For a rotationally symmetric cell in 3D, maintaining constant volume implies that the cell width must scale approximately with the inverse square root of cell height. For a 2D apico-basal cross section of the same cell, maintaining constant cross-sectional area implies that the width must scale approximately with inverse of the height. In 2D simulations, this will artificially amplify the effects of mesectoderm epiboly in Step 1 and make it more difficult to maintain narrow endoderm apices as the endoderm shortens in Step 2. To assess the extent to which this might bias our results, we ran simulations in which a constant area constraint was replaced by a constant cell volume constraint (assuming rotational symmetry of cells). We found that the tension parameter sets generating Step 1 and Step 2 solutions under a constant volume constraint were virtually identical to those employing the simpler 2D "volume" constraint (see Figure A4), suggesting that the errors we make by using 2D cross-sectional area as a proxy for volume can be ignored.

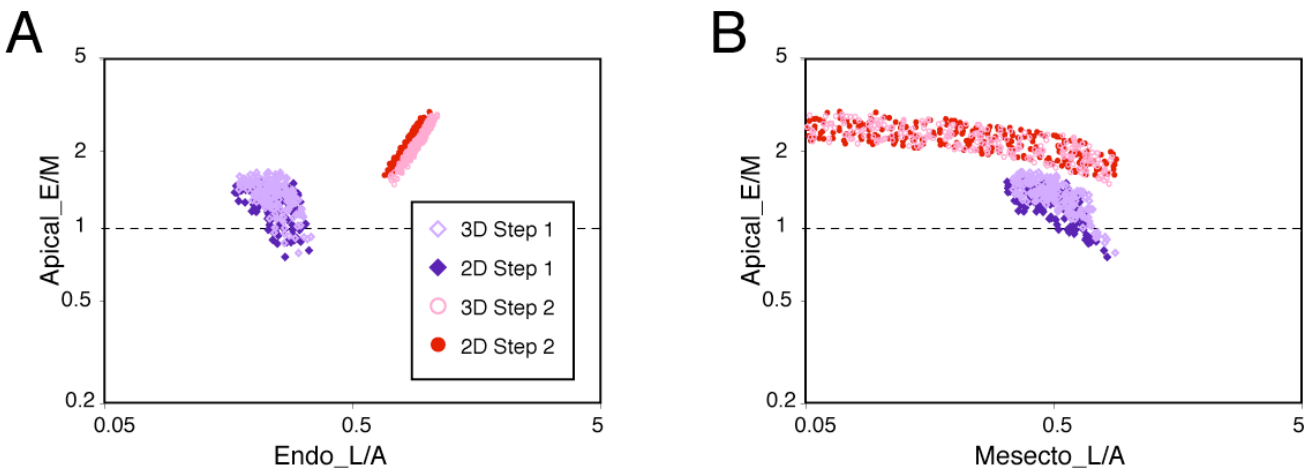

Figure A4. Comparison of parameter space searches using 2D and 3D measures of cell volume.

Panels A and B present the projections along the Mesecto-L/A and Endo-L/A axes, respectively, of successful parameters in 2D and 3D. Parameter space searches were performed as described in the main text and above, using identical starting geometries and target criteria. "2D" simulations used cross-sectional area of each model cell as the proxy for cell volume. "3D" simulations used the volume of a cell obtained by rotating the 2D cross-section about its centroid and perpendicular to its major axis (obtained by least squares fit of the cell outline to an ellipse).

2) Contributions from out-of-plane forces. For a row of identical cells in our 2D simulations (Figure A5), the outcome is entirely determined by the ratios of apical::basal::lateral tensions. The ratio of inner (lateral) to outer ($\sim \frac{T_{Apical} + T_{Basal}}{2}$) tensions control apico-basal height and lateral spread; the ratio of apical to basal tensions controls the tendency for the row to curve – inwards for $T_{Apical} > T_{Basal}$, outwards for $T_{Apical} < T_{Basal}$, no curvature for $T_{Apical} = T_{Basal}$.

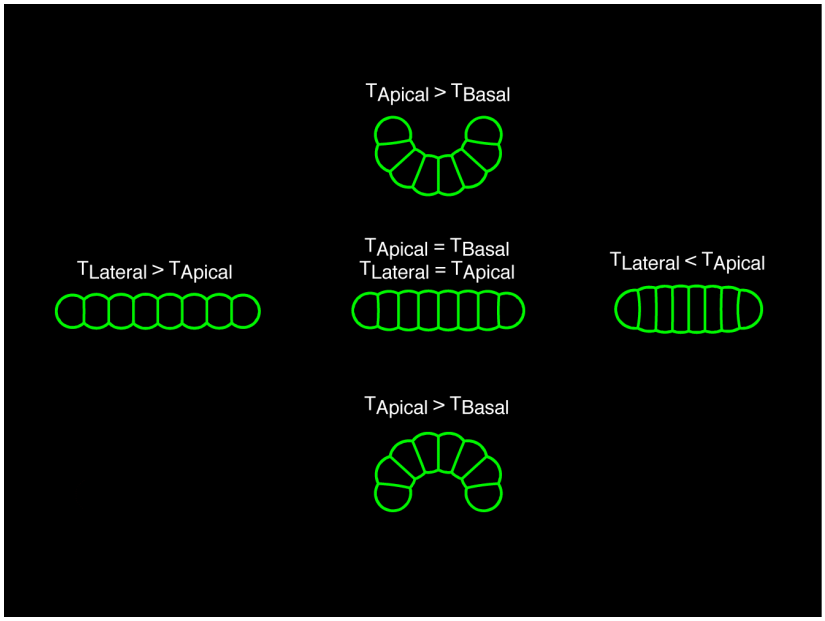

Figure A5. Relative tension values govern apico-basal height, width, and curvature of a model cell sheet. *All simulations were started from identical initial conditions and run for 500 model seconds.*

By symmetry, an analogous balance of apical, lateral and basal forces will control the tendency of a 3D sheet – e.g. the mesectoderm or the endoderm – to deform within any 2D cross-section. However, additional out of plane forces will also influence bending deformations of the sheet. A pair of cells positioned symmetrically with respect to the center of the 2D cross-section represents an annular ring of cells in 3D and bending of the sheet implies circumferential deformation of the ring. If the sheet maintains constant curvature and cross-sectional width, then increasing curvature implies

circumferential shortening (Figure A6).

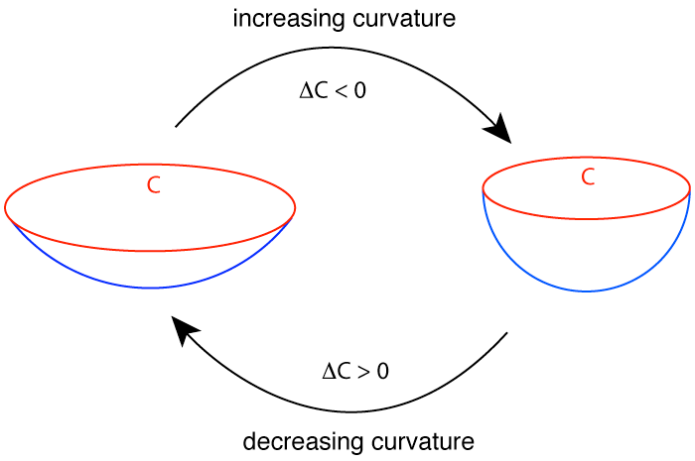

Figure A6. Schematic view of out-of-plane deformations associated with bending of the endoderm (or mesectoderm) sheet. *For a rotationally symmetric monolayer sheet that maintains constant width as it bends, the circumference must shorten as the sheet bends inward and lengthen as the sheet bends outward.*

Intuitively, resistance to compression of the ring should tend to oppose bending of the sheet. To test this and to assess the potential contribution of this resistance, we made a very crude simulation of a 3D sheet as follows: We represented the boundary of each cell in 3D as a collection of triangular elements, connected at common vertices. We represented apical and basal surfaces of each cell with a single triangular element; lateral surfaces with 4 triangular tiles sharing a common central vertex (Figure A7).

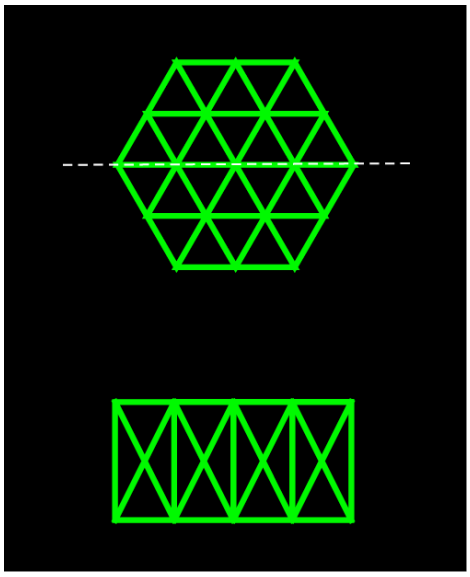

Figure A7. Architecture of a minimal 3D model of an isolated sheet of 24 cells. *On the left is a top view; on the right a lateral cross-sectional view. Each cell's apex and base is made of a single triangular element. Each lateral face is composed of 4 triangular elements that meet at a common vertex.*

We assumed isotropic contractile stress σ on each boundary element (different for apical, basal and lateral boundaries), and computed the contribution to each vertex using standard finite element methods (Zienkiewicz et al, 2005):

(11) $$\vec{F}_{cont} = \frac{-\sigma}{2}(L_{+}\hat{n}_{+} + L_{-}\hat{n}_{-})$$

where symbols (+) and (-) denote edges clockwise and counterclockwise to a given vertex, L is edge length, and $\hat{n}_i$ is the unit outward normal to an edge within the plane of the triangular element. We assumed constant cell volume maintained by a pseudo-pressure force, analogous to that used for the 2D simulations, acting on each triangular surface element:

(12) $$\vec{F}_{pressure} = \beta * A * \frac{V - V_0}{V_0}\hat{n}$$

where V is current cell volume, V_0 is the volume set point, A is the area of the triangular element, $\hat{n}$ is the unit outward normal to that element, and β is a constant. The net force acting on each vertex is thus:

(13) $$\vec{F}_{total} = \sum_i (F_{cont,i} + F_{pressure,i})$$

where the index ranges over all triangular elements sharing that vertex. In this crude analysis, we sought only to determine what shape the sheet will adopt at mechanical equilibrium for specific values of apical, lateral and basal stresses. Thus we neglected internal viscous resistance to deformations of

surface elements and used a simple first order Euler scheme to solve:

(14) $$\mu \frac{d\vec{x}_j}{dt} = \vec{F}_{total,\,j}$$

where $\vec{x}_j$ is the position of vertex j and μ is an arbitrary constant. We chose values for apical, lateral and basal surface stresses so that their ratios matched those for successful Step 2 simulations, then compared the results to 2D simulations of whole embryos and isolated 4-cell rows (Figure A8).

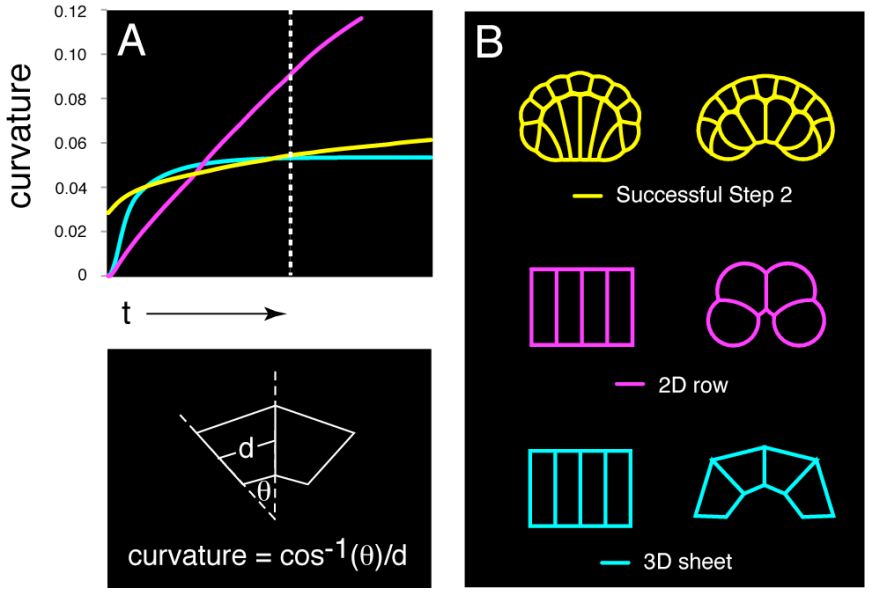

Figure A8. Comparison of 2D and 3D simulations. *(A) Plots of curvature vs simulation time for: successful Step 2 simulations (yellow), isolated row of 4 cells in 2D (magenta), 3D sheet of cells using ratios of boundary stresses identical to tension ratios used for Step 2 and 4-cell simulations (cyan). Vertical dashed line indicates last timepoint in Step 2 simulations. (B) Snap shots from simulations, showing (left) initial geometry and (right) geometry at the time point indicated by vertical dashed line in (A). Trajectories of 2D and 3D simulations are not directly comparable, but the final steady state shapes indicate that invaginations deeper than those seen in vivo or successful 2D Step 2 simulations can be achieved before out of plane forces limit further invagination.*

The comparison reveals several qualitative points: Comparing simulations of isolated 2D rows and 3D sheets for identical tension/stress ratios (cyan and magenta traces in Fig A8a; cross-sections in A8b), we find that there is no limit to how far a row of cells will bend in 2D, except steric limits that arise when the endpoints meet at the midline (Figure A8 and data not shown). In contrast, the 3D sheet asymptotically approaches an equilibrium shape in which the resistance to out-of-plane compression of circumferential rings balances the bending forces acting within the lateral cross-section. Thus circumferential forces limit the extent to which the sheet will bend in 3D, relative to the 2D case. However, the resistance to out-of-plane deformation (reflected as a decrease in the bending rate; cyan trace in Figure A8a) only becomes significant after the curvature of the sheet, and the depth of invagination, have reached extents comparable to those observed for endoderm cross-sections near the end of Step 2 simulations and in vivo (compare cyan and yellow traces in Fig A8a; cross-sections in Fig A8b; Figure 4C,M).

This (admittedly crude) analysis suggests that 2D simulations will tend to overestimate the depth of endoderm invagination slightly, and thus for full 3D simulations, we would expect the magnitudes of tension ratios required to match invaginations seen in live embryos to shift, but not by very much. In particular, because out-of-plane resistance would be expected to make it harder for the endoderm to invaginate either by apical contraction alone or by a combination of apical and lateral contraction, neglecting its consequences in our 2D simulations should not affect our main conclusion - that in the context of a resisting mesectoderm, increasing apical endoderm tension alone cannot explain endoderm invagination, only an increase in both apical and lateral endoderm tension can do so.

The other main conclusion from our modeling is that the mesectoderm does not help drive, but rather

resists endoderm deformation. The resistance to out-of-plane compression of circumferential mesectoderm rings that we ignore in our 2D simulations would in fact tend to increase this resistance. Similar considerations may also explain why our 2D simulations predict more apical endoderm constriction in response to mesectoderm ablation than we measured in experimental mesectoderm ablations. In the experiments, we ablated the 10 central ectoderm cells leaving a ring of mesectoderm cells surrounding the endoderm plate. Resistance to circumferential compression of this ring (which we ignore in our 2D simulated ablations) would reduce apical constriction, all other things equal.

SUPPLEMENTARY REFERENCES

Bausch, A.R., Möller, W., and Sackmann, E. (1999) Measurement of local viscoelasticity and force in living cells by magnetic tweezers. Biophys J. 76:573-9.

Bray, D., and White, J.G. (1988) Cortical flow in animal cells. Science, 239, 883-8

Costa, M, Raich, W., Agbunag, C., Leung, B., Hardin, J., and Priess, J (1998) A putative catenin cadheirin system mediates morphogenesis of the Caenorhabditis elegans embryo. J Cell Biol, 141:297-308.

Dawes-Hoang, R.E., Parmar, K.M., Christiansen, A.E., Phelps, C.B., Brand, A.H., and Wieschaus, E. (2005). *folded gastrulation*, cell shape change, and the control of myosin localization. Development. *132*:4165-4176.

Lang, T., Wacker, I., Wunderlich, I., Rohrbach, A., Giese, G., Soldati,T., and Almers, W.(2000). Role of actin cortex in the subplasmalemmal transport of secretory granules in PC-12 cells. Biophys. J. 78, 2863–2877.

Howard, J. (2001) Mechanics of Motor Proteins and the Cytoskeleton. (2001). Sinauer Associates.

Lecuit, T. and Lenne, P. F. (2007) Cell surface mechanics and the control of cell shape,tissue patterns and morphogenesis. *Nature Rev. Mol. Cell. Biol.* **8,** 633-644.

Munro, E.M., Nance, J., and Priess, J (2004) Cortical flows powered by asymmetrical contraction transport PAR proteins to establish and maintain anterior-posterior polarity in the early *C. elegans* embryo. Dev. Cell, 7(3), 413-424.

Press, W.H., Flannery, B.P., Teukolsky, S.A., and Vetterling, W.T. (1992) Numerical recipes in C. The art of scientific computing. Cambridge University Press, Second edition.

Zienkiewicz, O.C., Taylor, R.L., Zhu, J.Z. (2005) The finite element method: Its basis and fundamentals. Wiley Academic press.

SUPPLEMENTARY FIGURES

Figure S1. **An interactive PDF file containing 3D reconstructions of the embryos shown in Figure 1.** Please download SupplementaryFigure1.pdf as a standalone file from the main supplementary info page.

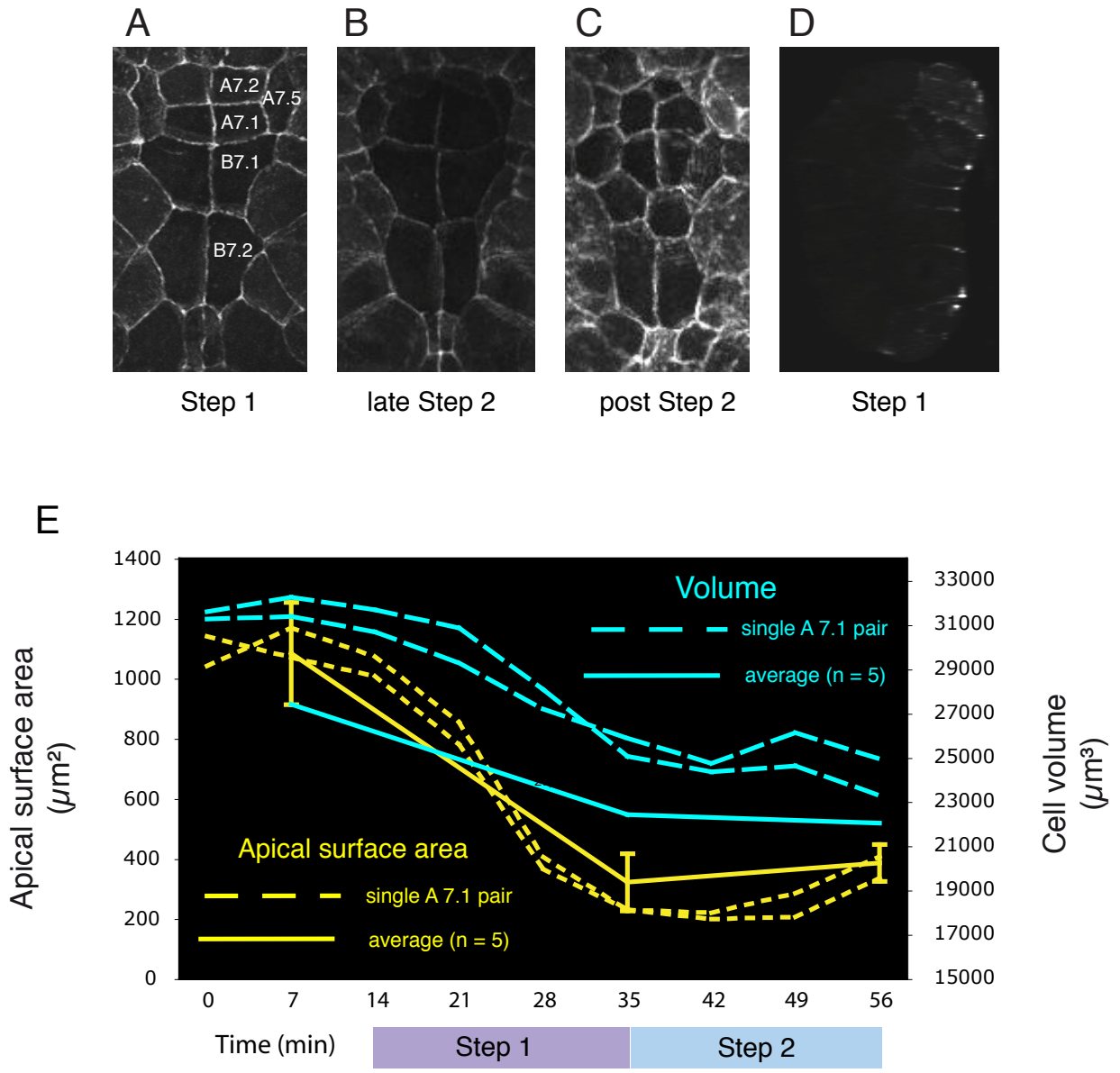

Figure S2. Supplementary architectural and morphometric analyses, related to Figure 2. A-D: Tight junctions are maintained during invagination. **(A-C)**: Confocal projections of a developing *Phallusia* embryo injected at egg stage with ZO-1-GFP mRNA, collected at (A) 76-cell stage, (B) late 112-cell stage and (C) just after division of the endoderm precursors (labeled post Step 2). All projections are centered on the endoderm. Labels in (A) indicate the endoderm precursors. **(D)** Sagittal section through the stack from which the projection shown in (A) was made, showing the apical

localization of ZO-1-GFP. **(E)** Changes in volume and apical surface area change in A7.1 endoderm cells during early gastrulation in *Phallusia*. Changes in volume (blue lines) mirror changes in apical surface area (yellow lines) in endodermal cells. Dashed lines represent values measured for a pair of A7.1 cells in a single live embryo. Solid lines represent the mean values for A7.1 cells measured in a sample of 5 fixed embryos. Error bars indicate standard deviations.

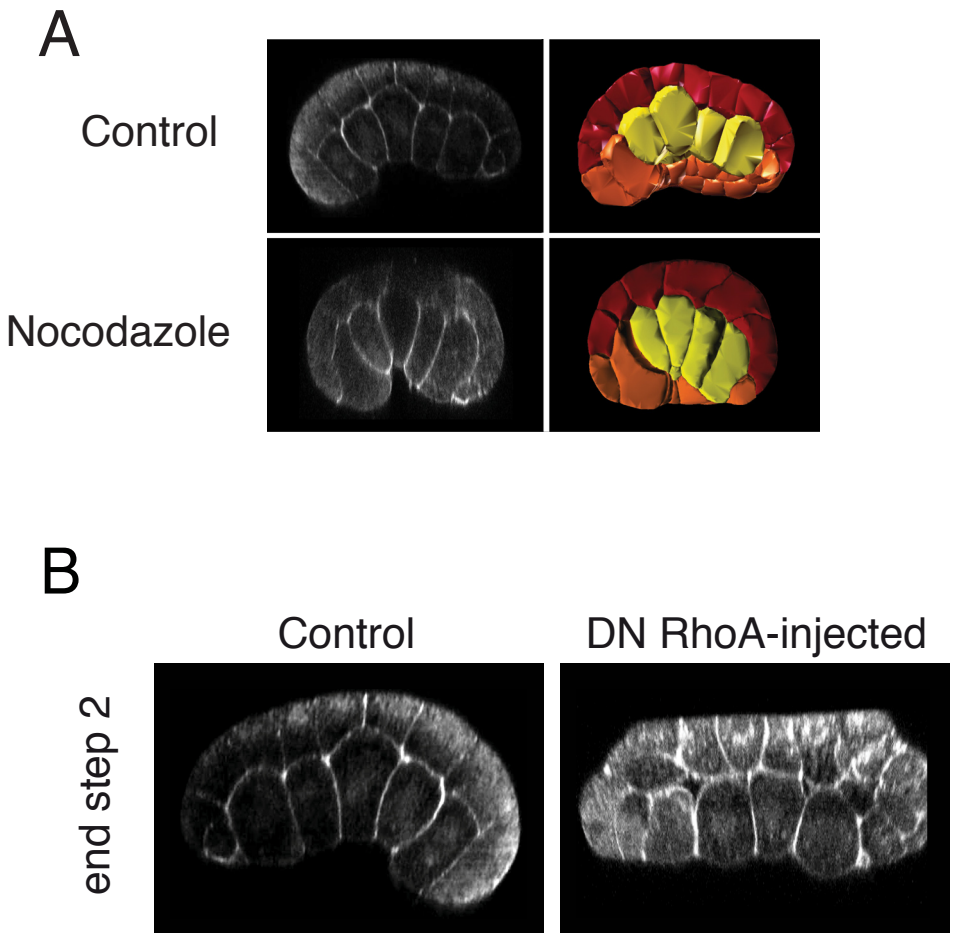

Figure S3. Further analyses of cytoskeletal requirements for invagination, related to Figure 4. (A) Microtubules are not required for invagination. Top panel: Control *Ciona intestinalis* embryo at the late 112-cell stage in sagittal view (left) and corresponding 3D reconstruction (right). Bottom panel: Embryo treated with 1.3μM Nocodazole from the 64-cell stage on and shown at late 112-cell stage in sagittal view and corresponding 3D reconstruction (right). **(B)** *Ciona intestinalis* embryos expressing DN RhoA shorten apico-basally, but fail to invaginate. Embryos were microinjected with mRNA encoding DN RhoA after fertilization and allowed to develop to the end of Step 2. Left Panel: Sagittal view of a control embryo at the end of Step 2. Right Panel: Sagittal view of a DN RhoA injected embryo at the end of Step 2. Note that in DN RhoA injected embryos, the endoderm cells shorten apicobasally to the same extent as wild type, but endoderm apices are expanded and the endoderm surface remains flat (un-invaginated).

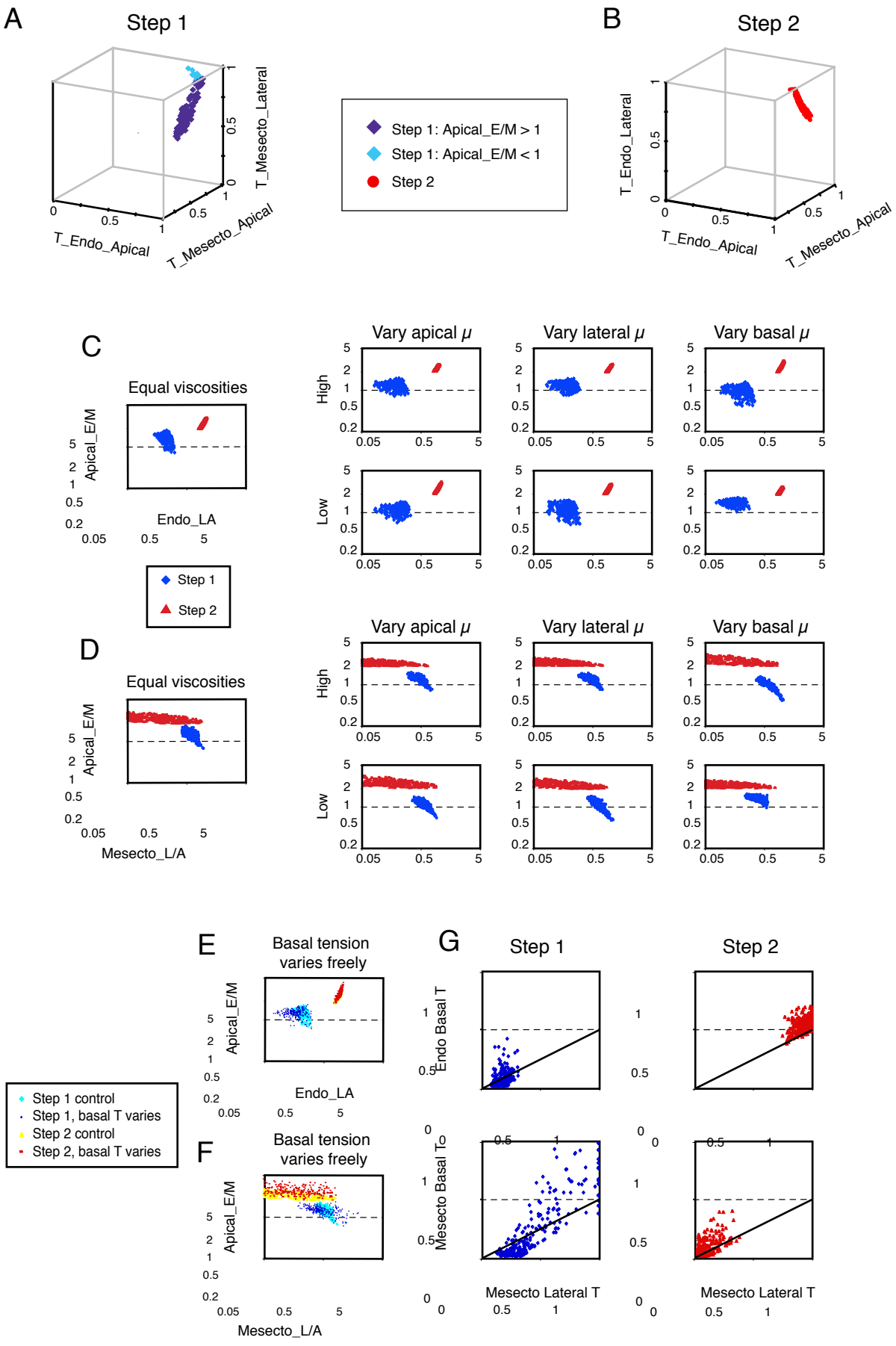
A
Step 1
T_Endo_Apical
T_Mesecto_Apical
T_Mesecto_Lateral
Step 1: Apical_E/M > 1
Step 1: Apical_E/M < 1
Step 2
B
Step 2
T_Endo_Lateral
T_Endo_Apical
T_Mesecto_Apical
C
Equal viscosities
Apical_E/M
Endo_LA
Step 1
Step 2
Vary apical μ
Vary lateral μ
Vary basal μ
High
Low
D
Equal viscosities
Apical_E/M
Mesecto_L/A
Vary apical μ
Vary lateral μ
Vary basal μ
High
Low
E
Basal tension varies freely
Apical_E/M
Endo_LA
F
Basal tension varies freely
Apical_E/M
Mesecto_L/A
Step 1 control
Step 1, basal T varies
Step 2 control
Step 2, basal T varies
G
Step 1
Step 2
Endo Basal T
Mesecto Basal T
Mesecto Lateral T
Mesecto Lateral T

Figure S4. Supplementary analyses of parameter space searches, related to Figure 5. **(A,B)** Plots showing relative values of individual boundary tensions for successful Step 1 (A) and Step 2 (B) parameter sets. Tension is measured in arbitrary units, and the maximum tension value is scaled to 1 for each parameter set. For Step 1 (A), when apical endoderm tension (T_Endo_Apical) is maximal (dark blue points), the mesectoderm apical and lateral tensions can vary widely, but their ratio (mesecto_LA) is roughly constant (see Figure 5F). For all other solutions (light blue points), T_Mesecto_Lateral increases as T_Endo_Apical decreases, and remains high relative to T_Mesecto_Apical, suggesting that mesectoderm epiboly can compensate for reduced apical constriction of endoderm during step 1. Step 2 solutions (B) follow a simpler constraint: both T_Endo_Apical and T_Endo_Lateral must be high relative to T_Mesecto_Apical. **(C,D)** Effects of varying effective internal viscosities on different boundaries. Internal viscosities on either all apical or all lateral or all basal (blastocoel) boundaries were set to 10x or 0.1x the values on the other boundaries. The maximum viscosity was fixed across all cases – i.e a relative 10x increase on particular boundaries was achieved by lowering values on all other boundaries to 0.1x. Left panels: Distributions of successful parameter sets for equal viscosities (replotted from Figure 5F,G to allow direct comparison) for Step 1 (blue) and Step 2 (red). C: Apical_EM vs endo_LA. D: Apical_EM vs ecto_LA. Right panels: Distributions of successful parameters for variable viscosities shown in identical format. Labels above plots indicate which viscosity was varied; labels at left indicate which direction: high = 10x; low = 0.1x. E-F: show distributions of successful parameters for Step 1 (blue) and Step 2 (red) obtained when basal (i.e. blastocoel) tensions are allowed to vary freely (instead of constraining basal tension to be 0.5x the corresponding lateral tensions). Compare directly to left panels in C&D. G: Plots of basal vs lateral tensions for endoderm (top panels) and mesectoderm (bottom panels) for Step 1 (left panels) and Step 2 (right panels).

Nocodazole
(Cleavage-arrest)

A

Starting geometries

Step 1 Step 2

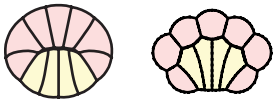

B

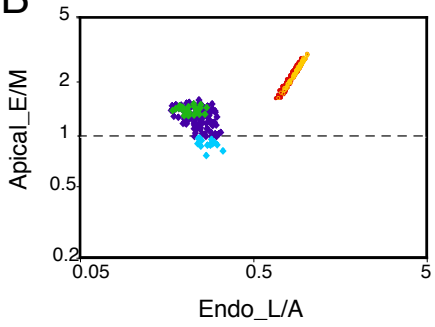

C

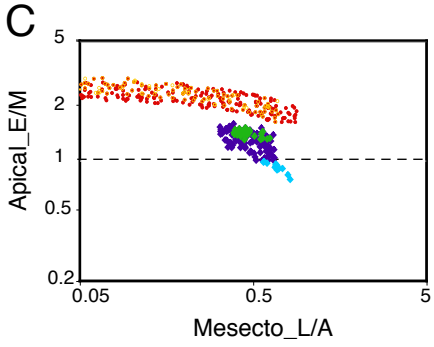

- Step 1 control: Apical_EM > 1
- Step 1 control: Apical_EM < 1
- Step 1 cleavage-arrest
- Step 2 control
- Step 2 cleavage-arrest

Blebbistatin

D

Step 1 Step 2

100μM Bleb.

Exp

Sim

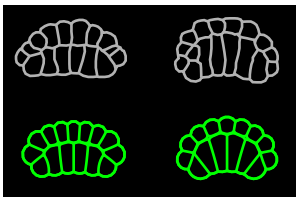

10% T_{max}

E

Endoderm height

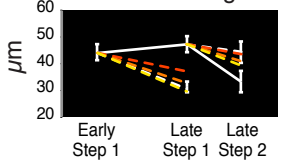

F

Endoderm apical width

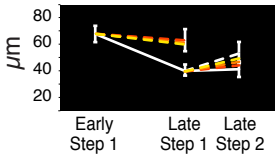

Experiment

Control

100μM Bleb

Simulation T_{Bleb} =

5% T_{max}

10% T_{max}

15% T_{max}

G

Invagination depth

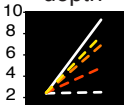

Y-27632

H

Step 1 Step 2

100μM Y-27632

Exp

Sim

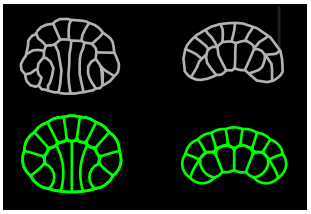

60% $EndoT_A$
40% $EndoT_L$

80% $EndoT_A$

I

Endoderm height

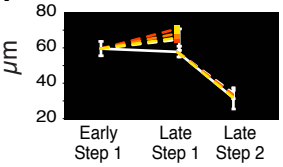

J

Endoderm apical width

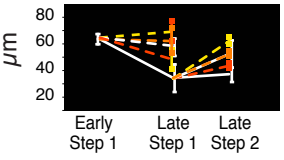

Simulation

Experiment

Control

100μM Y

Step 1

50% $EndoT_A$/25% $EndoT_L$

60% $EndoT_A$/40% $EndoT_L$

70% $EndoT_A$/55% $EndoT_L$

Step 2

70% $EndoT_A$

80% $EndoT_A$

90% $EndoT_A$

K

Invagination depth

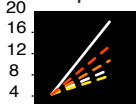

Figure S5. Further comparisons of experimental and simulated perturbations, related to Figure 6. **(A-C)** Matching simulations of invagination in cleavage-arrested embryos**. (A)** Starting geometry for simulations designed to mimic nocodazole-treated, cleavage-arrested embryos (passing criteria were the same as shown in Figure 5B for controls). (**B,C**) Position in parameter space of the subset of wild type solutions that also reproduce Step 1 and Step 2 in cleavage-arrested embryos (cf Figure S3A), shown as projections along the Mesecto_L/A (B) or Endo_L/A (C) axes and superposed upon normal solutions. The scales along the axes are logarithmical and the color legend applies to both panels. Note that the parameter sets that reproduce invagination in both normal and cleavage-arrested embryos are those (with apical_EM high and mesecto_LA low) for which apical endoderm contraction makes a maximal contribution relative to epiboly. **(D-K)** Simulations recapitulate morphological effects of Y-27632 or Blebbistatin. D-G: Blebbistatin treatment was simulated by reducing all cortical tensions to a single residual value $T_{bleb,}$ expressed as a fraction of the maximum tension in control simulations. **D**: Comparison of experimental and simulated (T_{bleb} = 10% T_{max}) morphologies for blebbistatin treatments during Step 1 and Step 2. For experimental embryos (gray), cell outlines were traced from the Blebbistatin-treated embryos shown in Fig 4B&D. **E-G**: Measurements of apico basal height, endoderm width and invagination depth for the 3 indicated values of T_{bleb} (dashed red, orange and yellow lines) relative to experimental controls (solid white lines) and blebbistatin-treated (dashed white lines) embryos. **H-K**: Y-27632 treatment was simulated by reducing endoderm apical and lateral tensions to fractions, $EndoT_{Y\_A}$ and $EndoT_{Y\_L}$ respectively, of their values for each of 100 passing/successful parameter sets. **H**: Comparison of experimental and simulated ($EndoT_{Y\_A}$ = 0.6 $EndoT_A$,$EndoT_{Y\_L}$ = 0.4$EndoT_L$) morphologies for Y treatments during Step 1 and Step 2. For experimental embryos (gray), cell outlines were traced from the Y-treated embryos shown in Fig 4L&N. **I-K**: Measurements of apico-basal height, endoderm width and invagination depth predicted for (F) Step 1 with the three indicated

combinations of $EndoT_{Y\_A}$ and $EndoT_{Y\_L}$ (dashed red, orange and yellow lines) and (G) Step 2 with the three indicated values of $EndoT_{Y\_A}$ (dashed red, orange and yellow lines) relative to experimental controls (solid white lines) and Y-treated (dashed white lines) embryos. Error bars indicate standard deviations.

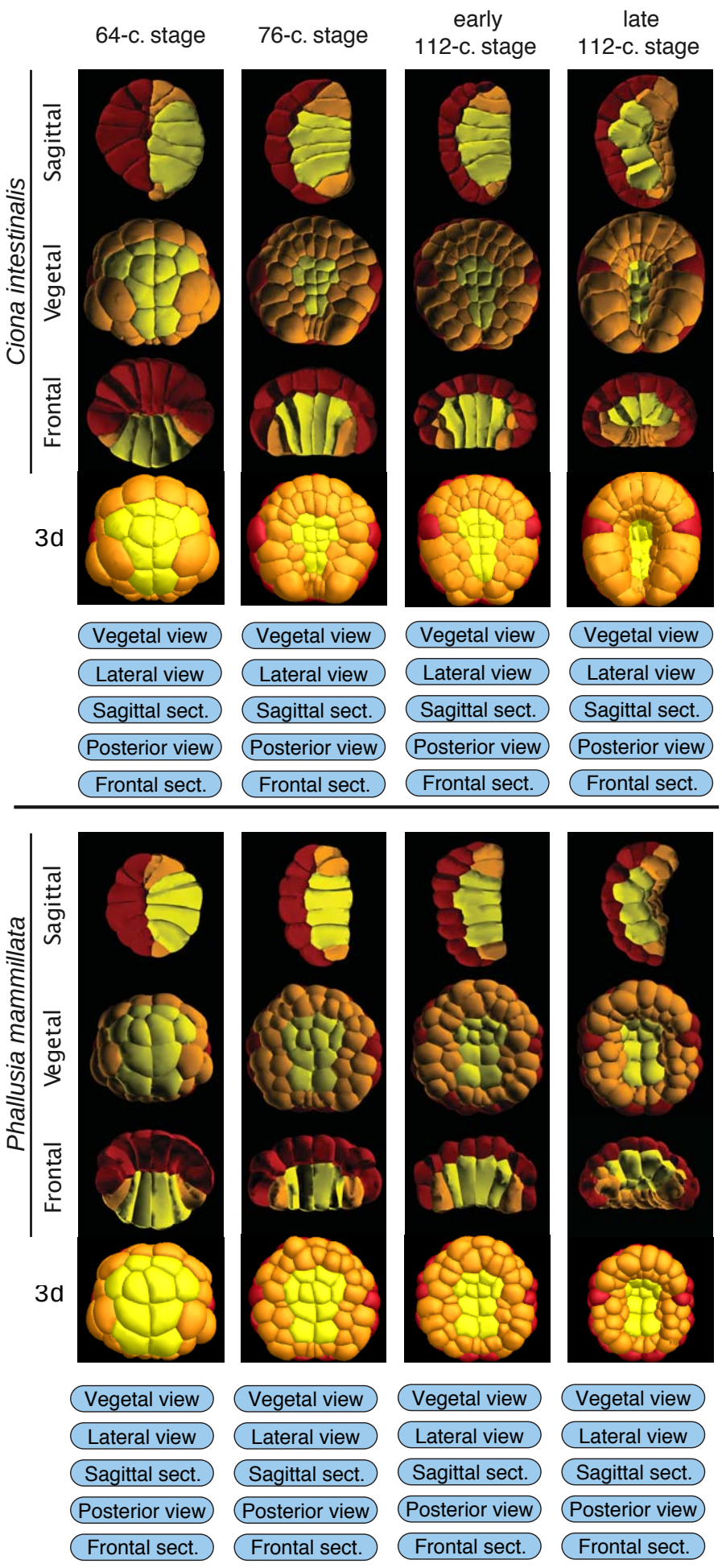

Supplementary Figure 1